Title

A warming-induced reduction in snow fraction amplifies rainfall extremes

Journal

Nature, 619(7969)

ISSN

0028-0836

Authors

Ombadi, Mohammed

Risser, Mark D

Rhoades, Alan M

et al.

Publication Date

2023-07-13

DOI

10.1038/s41586-023-06092-7

Article

A warming-induced reduction in snow fraction amplifies rainfall extremes

https://doi.org/10.1038/s41586-023-06092-7

Received: 26 October 2022

Accepted: 14 April 2023

Published online: 28 June 2023

Check for updates

Mohammed Ombadi[1,2]✉, Mark D. Risser[1], Alan M. Rhoades[1] & Charuleka Varadharajan[1]

The intensity of extreme precipitation events is projected to increase in a warmer climate[1–5], posing a great challenge to water sustainability in natural and built environments. Of particular importance are rainfall (liquid precipitation) extremes owing to their instantaneous triggering of runoff and association with floods[6], landslides[7–9] and soil erosion[10,11]. However, so far, the body of literature on intensification of precipitation extremes has not examined the extremes of precipitation phase separately, namely liquid versus solid precipitation. Here we show that the increase in rainfall extremes in high-elevation regions of the Northern Hemisphere is amplified, averaging 15 per cent per degree Celsius of warming—double the rate expected from increases in atmospheric water vapour. We utilize both a climate reanalysis dataset and future model projections to show that the amplified increase is due to a warming-induced shift from snow to rain. Furthermore, we demonstrate that intermodel uncertainty in projections of rainfall extremes can be appreciably explained by changes in snow–rain partitioning (coefficient of determination 0.47). Our findings pinpoint high-altitude regions as 'hotspots' that are vulnerable to future risk of extreme-rainfall-related hazards, thereby requiring robust climate adaptation plans to alleviate potential risk. Moreover, our results offer a pathway towards reducing model uncertainty in projections of rainfall extremes.

Global warming is anticipated to increase the intensity of extreme precipitation events[1–5], which could undermine infrastructure design and management assumptions in a future climate. The atmospheric holding capacity of water vapour increases at a rate of approximately 7% per 1 K of warming (as specified by the Clausius–Clapeyron (C–C) relationship), which drives corresponding increases in extreme precipitation events[3,12–14]. In addition, local and large-scale dynamical factors have been identified as complementary mechanisms for increases in precipitation extremes[4,15,16]. In addition to increases in the intensity of precipitation extremes, a warmer climate will assuredly alter the partitioning of precipitation into liquid and solid forms. More specifically, the snow fraction (the proportion of precipitation falling as snow) is projected to decrease for most regions of the globe[17–20]. This decrease is evident for both mean and extreme precipitation, albeit with lower rates for extreme precipitation[19]. In the present study, we solely focus on the snow fraction of precipitation extremes.

In light of anticipated increases in precipitation extremes and lower snow fractions in a warmer climate, it is reasonable to consider the combined effect of both changes on rainfall (liquid precipitation) extremes. The importance of this stems from the devastating impacts of rainfall extremes. Unlike snowfall, rainfall triggers runoff more rapidly, leading to a higher risk of flooding[6], landslide hazards[7–9] and soil erosion[10,11]. For instance, rainfall-driven floods in western United States were found to be 2.5-times greater than those driven by snowmelt[6] and are expected to become more frequent in the coming century as snowfall transitions to rainfall[21]. In addition, rainfall is considered to be the main driver of landslides[8], hence it is often incorporated in the assessment of landslide hazards[22,23], particularly after major fire events[24]. It is because of these reasons that civil engineers have typically designed infrastructure to withstand extreme rainfall events as opposed to extreme total precipitation (liquid and solid) events[25,26]. As previous studies on precipitation extremes have not considered the partitioning of rain and snow, it remains largely unknown, both qualitatively and quantitatively, whether and how a reduction in the snow fraction might change the risk of rainfall extremes over specific parts of the globe.

Here we show that the increase in rainfall extremes is amplified in high-altitude regions and in regions that receive a considerable amount of their annual precipitation as snow (snow fraction). We demonstrate this using both the fifth generation European Centre for Medium-Range Weather Forecasts atmospheric reanalysis (ERA5[27]) for the recent past (1950–2019) and future projections obtained from eight Earth-system models (Extended Data Table 1) participating in the Coupled Model Intercomparison Project Phase 6 (CMIP6). Moreover, we assess the sensitivity of our findings to different levels of global warming (+1.5 K, +2 K, +3 K and +4 K) resulting from different emissions scenarios (ssp126, ssp245, ssp370 and ssp585) using a total of 43 model simulations (Extended Data Table 3). Our results show that a reduction in the snow fraction amplifies rainfall extremes in snow-dominated regions and can explain 25% to 40% of the total spatial variability in the increase of rainfall extremes. We then demonstrate that intermodel uncertainty in the projection of increases in rainfall extremes is mainly

[1]Earth and Environmental Sciences Area, Lawrence Berkeley National Laboratory, Berkeley, CA, USA. [2]Department of Climate and Space Sciences and Engineering, University of Michigan, Ann Arbor, MI, USA. ✉e-mail: ombadi@lbl.gov

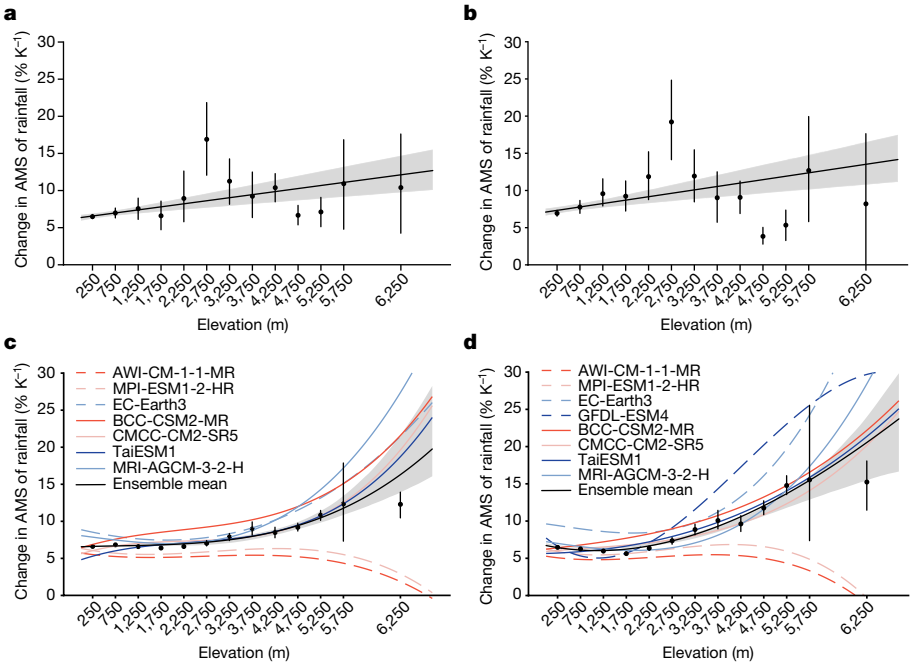

Fig. 1 | Elevation-dependent amplification of rainfall extremes. Percentage change in rainfall extremes, normalized by degrees of warming and expressed as a function of elevation over the spatial domain 20° N–90° N land area with masking of hyperarid regions (Methods). **a**, Three-hour annual maximum series (AMS) of ERA5 rainfall (slope of regression 0.82 (% per 1,000 m)). **b**, Daily AMS of ERA5 (slope of regression 0.92 (% per 1,000 m)). **c**, Three-hour AMS of CMIP6 models. **d**, Daily AMS of CMIP6 models. For **c** and **d**, the coloured dashed and solid lines correspond to different CMIP6 models as shown in the legend, and the black solid line represents the multimodel mean. Percentage change is calculated using the period 2071–2100 for CMIP6 models and the period 1950–1979 for ERA5. In all panels, regression is based on all grid cells within the spatial domain (not shown in the figure), and the shaded area surrounding the regression lines represents the 95% confidence interval of regression estimates. The black markers and error bars show the mean percentage change at different elevation categories and its 90% confidence interval for ERA5 (**a**,**b**) and CMIP6 multimodel mean (**c**,**d**). The elevation categories are: 0–500 m, 500–1,000 m, ..., 5,500–6,000 m and 6,000–8,000 m. The black markers and lines are drawn at the midpoint of each category; see Methods for details.

attributed to differences in the snow-fraction changes across models, and we conclude by estimating the increased risk of rainfall extremes in a warmer climate across different mountainous regions of the Northern Hemisphere using extreme-value analysis.

Elevation-dependent amplification

We first examine the increase in rainfall extremes over the spatial domain 20° N–90° N as a function of elevation (metres above sea level) for both ERA5 (Fig. 1a,b) and CMIP6 models (Fig. 1c,d). For ERA5 and CMIP6 models, the percentage change in rainfall extremes is computed using the two periods 1990–2019 and 2071–2100, respectively, relative to the baseline period of 1950–1979. In all panels of Fig. 1, the percentage change in rainfall extremes is normalized by the degrees of warming (% K^{-1}) in global average surface air temperature (over both land and oceans). Figure 1a,b shows a generally positive relationship between elevation and the increase in rainfall extremes with slope of regression line of 0.82 (% per 1,000 m; 0.4–1.2, 95th confidence interval) for 3 h, and 0.92 (% per 1,000 m; 0.4–1.4, 95th confidence interval) for 24 h. Similarly, Fig. 1c,d shows an elevation dependence in the increase of rainfall extremes obtained from the eight CMIP6 models (coloured dashed lines) and their multimodel mean (black line and markers). It is noteworthy that these relationships are consistent irrespective of the duration of rainfall extremes (3 h and 24 h as shown in Fig. 1 and 12 h in Extended Data Fig. 1a,b).

Although the results from ERA5 show a generally increasing trend, there are deviations from the regression line, especially at the elevation band of 2,500–3,000 m. There are several possible explanations for these deviations. First, the signal-to-noise ratio for differences between the two periods of 1990–2019 and 1950–1979 is not large owing to a relatively limited global warming level of +0.81 K, as estimated from ERA5 (Extended Data Table 2). Second, these deviations might be attributed to the lack of spatiotemporal homogeneity (particularly at certain elevation bands) in the observational inputs to ERA5 over the time period 1950–2019, which may lead to spurious trends unrelated to climate change[28]. Lastly, there may be a physical explanation wherein the 2,500–3,000 m elevation band experiences the greatest change in snow-to-rainfall partitioning in a warmer climate, although this effect is not evident in the CMIP6 projections (Fig. 1c,d). Contrary to ERA5, the high warming levels at the end of the century (2071–2100), ranging between +3.9 K and +6.6 K (Extended Data Table 2), induces a very strong signal. Overall, it is evident that both the reanalysis dataset and the CMIP6 models indicate an amplification of rainfall extremes at higher elevations. More specifically, the increase in rainfall extremes at high elevations (greater than 2,000 m) exceeds that of C–C scaling (7% K^{-1}), with average values as high as 15% K^{-1}.

Sensitivity to global warming

The percentage change in rainfall extremes shown in Fig. 1 is normalized by degrees of warming and expressed in units of (% K^{-1}) to account for differences in warming levels among CMIP6 models (Extended Data Table 2). Despite this normalization, it is conceivable that the results are biased by the inclusion of models that are oversensitive to greenhouse gas emissions, also known as 'hot models'[29]. Therefore, we assessed the sensitivity of our findings to different global warming levels of +1.5 K, +2 K, +3 K and +4 K relative to the reference period (1950–1979). This was carried out using a total of 43 CMIP6 model simulations shown in Extended Data Table 3, spanning 7 models and 4 emissions scenarios (ssp126, ssp245, ssp370 and ssp585), each with a sufficiently long period for statistical inference of 30 years that fall within the 2018–2100 period (see Methods for details). Figure 2a shows the distribution of

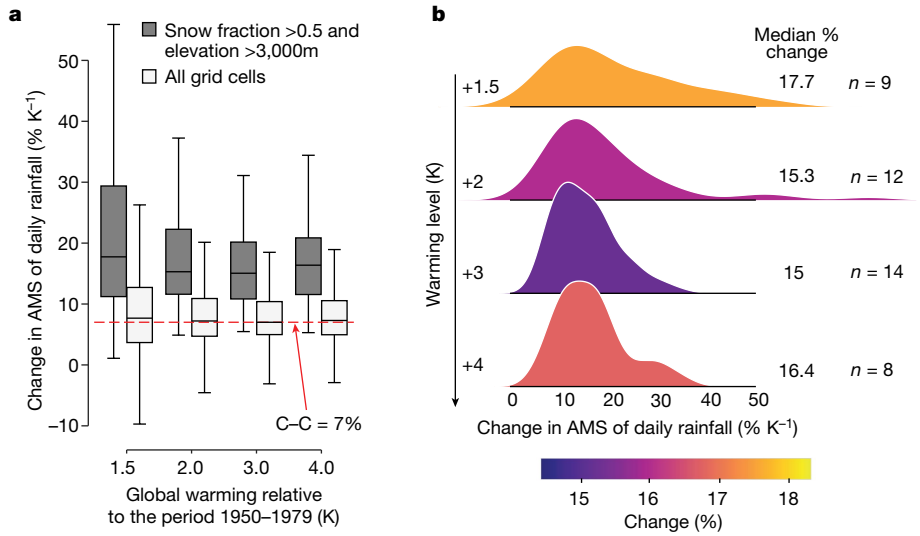

Fig. 2 | Sensitivity to global warming levels. a, Percentage change in annual maximum series (AMS) of daily rainfall obtained from a multimodel mean corresponding to each warming level (+1.5 K, +2 K, +3 K and +4 K). Details of ensemble members are provided in Extended Data Table 3. White-coloured boxes show results aggregated across all grid cells within the spatial domain of analysis (20° N–90° N) with masking of hyperarid regions (Methods). Dark-coloured boxes show values aggregated over grid cells with elevation >3,000 m and snow fraction >0.5. The boxes show the interquartile range (IQR; 25th percentile to 75th percentile) and the whiskers show the extent of the distribution excluding outliers defined as values greater than (75th percentile + 1.5 × IQR) or lower than (25th percentile − 1.5 × IQR). The red dashed line indicates the C–C scaling of 7% K^{-1}. **b**, The same as the dark-coloured boxes in **a** for regions with elevation >3,000 m and snow fraction >0.5, but visualized as Kernel distribution estimation plots to assess differences in more detail. The number of CMIP6 models used in each ensemble, denoted by *n*, is shown next to each distribution.

percentage change in daily rainfall extremes obtained from a multimodel mean corresponding to four different warming levels (+1.5 K, +2 K, +3 K and +4 K). Irrespective of warming level, the median increase across all grid cells is approximately 7% K^{-1}, which is consistent with both the C–C relationship and the observation-based analysis[30]; however, the increase over grid cells with elevation >3,000 m and snow fraction >0.5 is amplified, ranging between 15% and 17.7%. The distributions of percentage change in these regions (elevation >3,000 m, snow fraction >0.5) are shown in more detail in Fig. 2b. Apart from small differences in the tails of distributions, it can be clearly seen that the patterns of amplification in rainfall extremes are qualitatively similar regardless of warming level, with median values of 17.7% K^{-1}, 15.3% K^{-1}, 15.1% K^{-1} and 16.4% K^{-1} for warming levels of +1.5 K, +2 K, +3 K and +4 K, respectively. Given that these results are relatively insensitive to the level of warming, we focus on using only end-of-the century CMIP6 ssp585 model simulations (Extended Data Table 1) for the remainder of this article.

Spatial variability of rainfall extremes

To further attribute amplified rainfall extremes to changes in snow fraction, we examine the relationship between changes in snow fraction and the increase in rainfall extremes at the grid-cell level within each model. The scatter plots for this relationship are shown for each model and duration of 3 h, 12 h and 24 h in Extended Data Figs. 3 and 4. The Pearson correlation coefficient (ρ) values for these relationships are summarized in Fig. 3b. Across all models and rainfall durations, the values of ρ range from −0.28 to −0.64 with a median value of −0.46, −0.44 and −0.51 for rainfall durations of 3 h, 12 h and 24 h, respectively. These correlations provide explanatory power (-0.28^2 = 8% to -0.64^2 = 41%) regarding spatial variability patterns, which are remarkably strong given that they represent only a single factor among many that can shape spatial variability changes in precipitation (and rainfall) extremes.

A competing hypothesis that might explain the amplification patterns shown in Figs. 1 and 2 is related to potential changes in timing of precipitation extremes (that is, the occurrence of precipitation extremes shifting towards the warm season). Such a hypothesis can be ruled out based on findings from previous studies[31,32]. More specifically, analysis of vertically integrated saturation specific humidity related to precipitation extremes[31] and analysis of daily precipitation extremes from CMIP5 models[32] indicate a shift in timing of precipitation extremes towards the cold season. Furthermore, we carried out an analysis focusing on the daily timescale to quantify the magnitude of shift in timing of precipitation extremes. Figure 3c shows the cumulative distribution functions (CDFs) of changes in the timing of extremes at grid cells within each model. Across all models, 80% of grid cells show a change in the timing of extremes that is less than 20 days (GFDL-ESM4 model) to 40 days (CMCC-CM2-SR5 model). These results indicate that the magnitude of the shift in timing of precipitation extremes is not substantial and, together with previous findings[31,32] and the results in Fig. 3b, they suggest that changes in snow fraction are indeed a primary factor leading to amplified rainfall extremes at higher elevations.

Intermodel uncertainty of projections

It is clear from Fig. 1c,d that all models but two (MPI-ESM1-2-HR and AWI-CM-1-1-MR) show an amplified increase in rainfall extremes with elevation. Among the remaining models, the projections differ quantitatively. It is, therefore, informative to examine whether intermodel uncertainty could be attributed to differences in the models' projections of changes in the snow fraction. Figure 3a shows the relationship between the change in snow fraction in daily rainfall extremes for the period 2071–2100 relative to 1950–1979 averaged over the entire spatial domain for each model (horizontal axis), and the increase in rainfall extremes for each model (vertical axis). When averaged over the entire spatial domain (blue line and markers), changes in snow fraction can explain intermodel differences (slope 4.3% per 0.1 decrease in snow fraction, coefficient of determination R^2 = 0.47). The relationship is steeper over high-elevation regions (orange line and markers, slope 7.6% per 0.1 decrease in snow fraction, R^2 = 0.28). Interestingly, the peculiarity of the two models (MPI-ESM1-2-HR and AWI-CM-1-1-MR) may be partly explained by their low values of change in the snow fraction in extreme precipitation. In addition to this, both models underestimate the snow

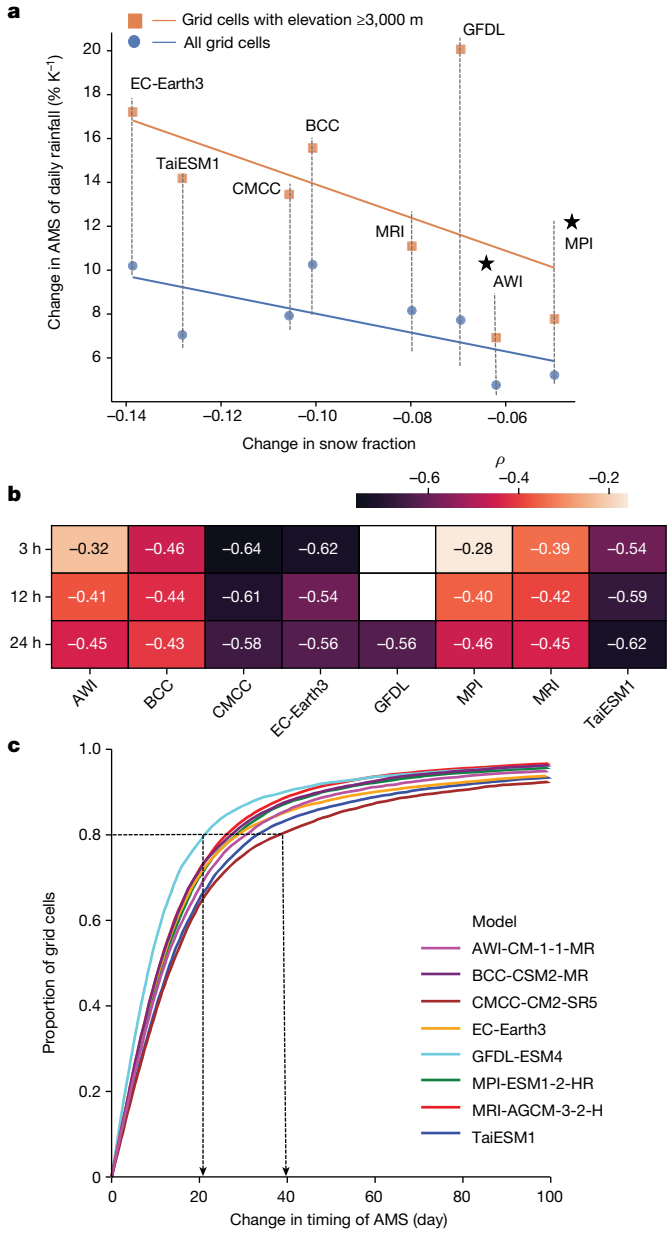

Fig. 3 | Reduction in snow fraction amplifies rainfall extremes. a, Scatter plot for the relationship between change in snow fraction of extremes and increases in daily rainfall extremes averaged over grid cells for each model. The solid lines are the least-squares linear regression. The blue and orange colours correspond to data averaged over all grid cells and grid cells with elevations ≥3,000 m, respectively. The two models AWI-CM-1-1-MR (AWI) and MPI-ESM-1-2-HR (MPI) are highlighted with an asterisk owing to their peculiar behaviour of lacking elevation-dependent amplification. **b**, Heatmap summarizing the values of correlation coefficient (ρ) for the relationship between change in snow fraction and change in rainfall extremes for grid cells within each model for rainfall duration of 3 h, 12 h and 24 h. Scatter plots for this relationship are shown in Extended Data Figs. 3 and 4. It is noted that the model GFDL-ESM4 (GFDL) has only 24-h rainfall estimates. **c**, CDFs for the change in timing of daily precipitation extremes over all grid cells within each model (Methods). The coloured lines correspond to different CMIP6 models as shown in the legend. The models with the lowest and highest shift in time for 80% of grid cells are highlighted with black dotted lines and arrows pointing to the change in annual maximum series (AMS) timing on the horizontal axis.

fraction in the baseline period (1950–1979) compared with ERA5 and other models (Extended Data Fig. 2a). These results provide preliminary clues that improving schemes of snow–rain partitioning could considerably reduce intermodel uncertainty in projections of rainfall extremes[33]; however, a comprehensive model diagnosis for uncertainty in projections of rainfall extremes is beyond the scope of this study.

Future risk of rainfall extremes

To assess the future risk of rainfall extremes in a warmer climate, we carried out an extreme-value analysis on the annual maximum series (AMS) obtained from the eight CMIP6 models (Methods). One way to quantify changes in the probability of exceeding a fixed threshold of extreme rainfall is via the risk ratio (see, for example, refs. 34,35), which summarizes the ratio of return probabilities for two periods of interest (here, the ratio of end of century versus the historical baseline). Figure 4a shows a map of the CMIP6 multimodel mean risk ratio (RR) for daily rainfall extremes where the threshold of interest is the 20-year return value as estimated from the reference period (Methods). An RR of 1 means that the future return probability is estimated to be 1/20 (that is, the future return period is 20, with no change in frequency), whereas an RR of 4 means that the future return probability is projected to increase to 1/5 (RR = (1/5)/(1/20); that is, higher frequency). It can be clearly seen that the Himalayas, the North American Pacific mountain ranges (Cascades, Sierra Nevada and Coastal ranges) and high-latitude regions exhibit a higher future risk of more frequent rainfall extremes (RR ≥ 7; dark blue colours on the map).

The relationship between RR and elevation is explicitly distilled in Fig. 4b. The figure shows the RR value for daily rainfall averaged for each 500-m elevation band (for example, 0–500 m, 500–1,000 m, ..., 5,500–6,000 m). In addition to showing the RR corresponding to the baseline 20-year return value, results for less extreme events (2-year, 5-year and 10-year return values) are also shown. It is clear that there is an elevation-dependent progression towards higher risk for the most extreme rainfall events (10-year and 20-year return values). It is noted that the RR for less extreme events such as the 2-year return value also increases with elevation albeit with a lower rate. To visualize the increase of 2-year RR with elevation, Extended Data Fig. 5a–c shows $\log_{10}$(RR) for rainfall duration of 3 h, 12 h and 24 h, respectively. Furthermore, Extended Data Fig. 5d,e shows the values of RR across different elevation bands for rainfall duration of 3-h and 12-h, respectively, which are consistent with those of 24-h rainfall duration. To further highlight regional differences in RR, Fig. 4c contrasts the distribution of RR values over non-snowy plains (elevation ≤200 m with no snow) with that of snow-dominated regions (mean annual snow fraction ≥0.5). The mean values for the two groups are 3.1 and 6.9, respectively. The difference is statistically significant (Welch's t-value = 47.1; $P < 0.001$). In addition, Fig. 4c shows the distribution of RR values for different mountain ranges in the Northern Hemisphere. The boundaries and spatial extents of these mountain ranges are shown in Extended Data Fig. 6. Clearly, the RR values are higher over mountain ranges (median 3.7–5.7) compared with that of non-snowy plains (median 3.1). The differences in RR among mountain ranges suggest regional variability in the amplification of rainfall extremes; for instance, the North American Pacific and Asian mountain ranges exhibit a higher RR than other mountain ranges, which could possibly be due to distinct mechanisms such as dynamically driven atmospheric changes on the Asian monsoon in the case of the Asian mountain ranges[31] and thermodynamically dominated changes to atmospheric rivers in the case of the North American Pacific[36]. However, a thorough evaluation of the models used herein simulating monsoons and atmospheric rivers is needed to prove causality of such results.

Discussion

Our findings provide several lines of evidence demonstrating a warming-induced amplification of rainfall extremes at high altitudes, specifically in snow-dominated regions of the Northern Hemisphere. As a result, these regions are regarded as 'hotspots' that are vulnerable to

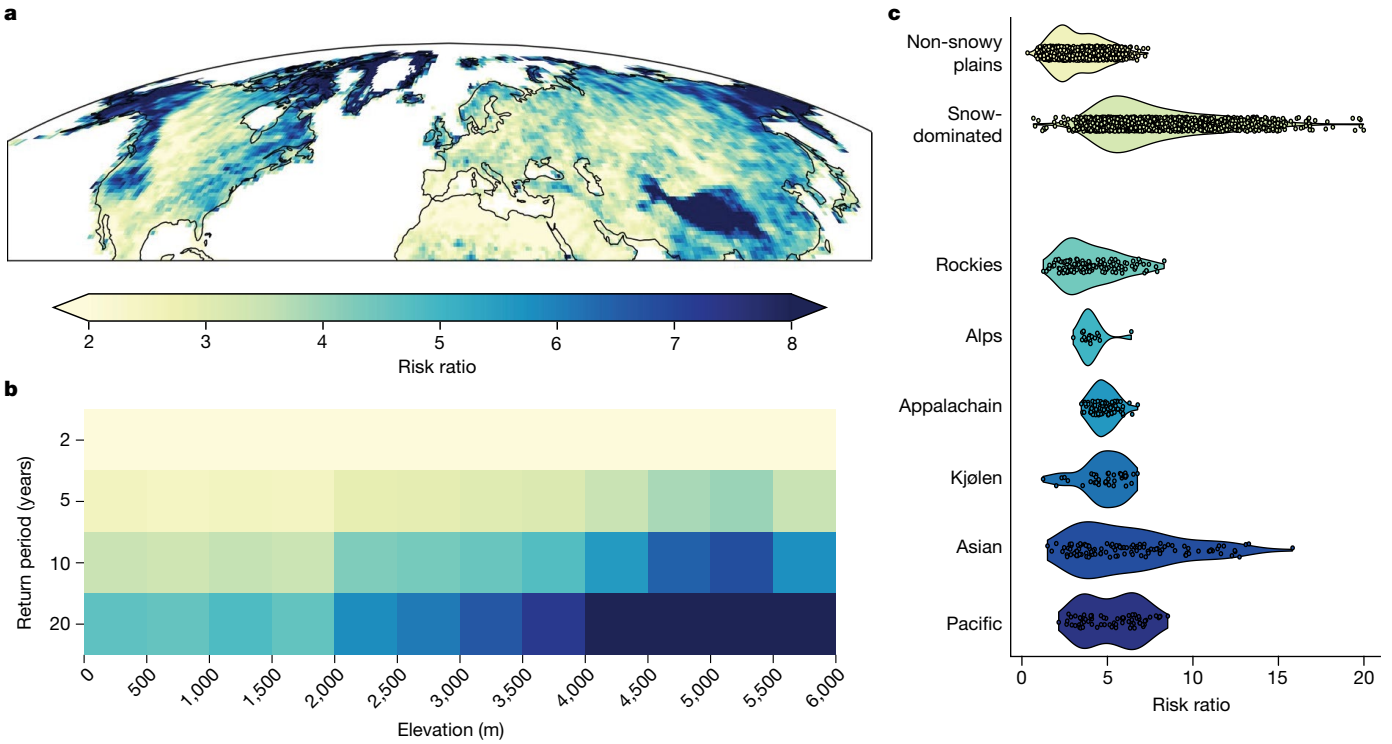

Fig. 4 | Projected risk of rainfall extremes. a, The multimodel mean value of RR for the 20-year return value of daily rainfall extremes (as estimated from the reference period) over the spatial domain 20° N–90° N. **b**, A heatmap of RR for daily rainfall extremes. Values are averaged for grid cells at each elevation category (for example, 0–500 m, 500–1,000 m and so on). The panel shows an RR corresponding to *T*-year return values for $T = 2$ years, $T = 5$ years, $T = 10$ years and $T = 20$ years. **c**, The values of RR for the 20-year return value of daily rainfall extremes (as estimated from the reference period) grouped for different mountain ranges (Rockies, Alps, Appalachian, Kjølen, Asian and Pacific). The spatial extent of mountain ranges is shown in Extended Data Fig. 6. In addition, the values of RR are grouped for non-snowy plains (elevation less than 200 m with no snow) and snow dominated (mean annual snow fraction greater than 0.5). The map in **a** was generated using Cartopy[47].

high risk of extreme rainfall events and their related hazards of flooding, landslides and soil erosion. The implications of our results centre around the importance of developing sound climate adaptation plans to protect the natural and built environments and the 26% of the global population living in or directly downstream of mountainous regions[15,37]. It is also important to recognize that the amplification of rainfall extremes is likely to be associated with a decrease in snowfall extremes owing to the transition from snow to rain. Such a decrease in snowfall extremes is consistent with previous work[19], and it presents an additional layer of complexity that needs to be taken into account in developing adaptation and mitigation strategies. In addition, in line with previous research on the invalidity of the stationarity assumption in water resources management[38–40], our findings emphasize the need for incorporating non-stationarity in the development of intensity–duration–frequency curves for resilient design of infrastructure in a future climate. Although previous research recognized the non-stationarity of precipitation extremes owing to the C–C relationship and other factors such as the feedback effect of convective clouds[41], we show in this study that non-stationarity effects are also affected by the transition of snow to rain, with a more pronounced change in high-altitude and snow-dominated regions, thereby requiring innovative and resilient infrastructure design. The additional future risk of rainfall extremes attributed to factors other than the C–C relationship can be quantified by comparing the RR values in Fig. 4 with those obtained from C–C-only increase (Methods). Extended Data Fig. 5f shows that this additional risk exceeds 50% in high-elevation regions. We, therefore, specifically call for updating intensity–duration–frequency curves in these hotspot regions to cope with future risk of extreme-rainfall-related hazards to ensure that infrastructure can be managed in a more real-time manner[42]. Furthermore, our results offer a paradigm in understanding regional differences associated with the intensification of rainfall extremes, complementing earlier paradigms in studying precipitation extremes such as zonal analysis based on latitude bands[4,43] and the dry-get-drier, wet-get-wetter framework[5].

In this study, we limited our analysis to the spatial domain of 20° N–90° N, excluding the tropics owing to uncertainties in model projections of tropical precipitation[4]. Also, the Southern Hemisphere was not considered here, mainly owing to the paucity of in situ observations in the pre-satellite era (before 1979), which could lead to biases in estimates of the baseline period (1950–1979). Such a lack of in situ observations is specifically more common in mountainous regions[44]. Although our results are consistent for both daily and subdaily rainfall extremes, there might be uncertainties in the latter owing to the inadequacy of convection-parameterized models in simulating subdaily extremes[44]. The robustness of our results is dependent on the spatiotemporal accuracy of the ERA5 reanalysis dataset and the eight Earth-system models used in this study to estimate extreme precipitation events and their snow–rain partitioning. It is worthwhile to note that systematic biases of underestimation and overestimation in rainfall extremes over the historical record are less of a concern in the present study. This is because each dataset is compared relative to its historical values over a comparable reference period to evaluate changes in extreme precipitation and snow fraction. On the contrary, errors in snow–rain partitioning and their changes with warming are potential sources of uncertainty[33]. In the present study, we evaluated daily rainfall extremes of ERA5 against ground observations from the Global Historical Climatology Network daily (GHCNd) dataset[45] (Methods and Extended Data Figs. 7a,b and 8). The evaluation results show that ERA5 adequately estimates rainfall extremes, which is consistent with recent studies showing that ERA5 generally performs well in snow–rain

partitioning over most continents and specifically in high latitudes[46]. Furthermore, we have investigated the existence of amplification patterns in rainfall extremes in the GHCNd dataset. Extended Data Fig. 7c,d shows clues of an amplified increase in rainfall extremes with elevation in the GHCNd dataset despite potential uncertainties arising from non-uniform sampling of GHCNd stations.

Online content

Any methods, additional references, Nature Portfolio reporting summaries, source data, extended data, supplementary information, acknowledgements, peer review information; details of author contributions and competing interests; and statements of data and code availability are available at https://doi.org/10.1038/s41586-023-06092-7.

1. Kharin, V. V., Zwiers, F. W., Zhang, X. & Hegerl, G. C. Changes in temperature and precipitation extremes in the IPCC ensemble of global coupled model simulations. *J. Clim.* **20**, 1419–1444 (2007).
2. Sun, Y., Solomon, S., Dai, A. & Portmann, R. W. How often will it rain? *J. Clim.* **20**, 4801–4818 (2007).
3. Pall, P., Allen, M. R. & Stone, D. A. Testing the Clausius–Clapeyron constraint on changes in extreme precipitation under CO_2 warming. *Clim. Dyn.* **28**, 351–363 (2006).
4. O'Gorman, P. A. & Schneider, T. The physical basis for increases in precipitation extremes in simulations of 21st-century climate change. *Proc. Natl Acad. Sci. USA* **106**, 14773–14777 (2009).
5. Donat, M. G., Lowry, A. L., Alexander, L. V., O'Gorman, P. A. & Maher, N. More extreme precipitation in the world's dry and wet regions. *Nat. Clim. Change* **6**, 508–513 (2016).
6. Davenport, F. V., Herrera-Estrada, J. E., Burke, M. & Diffenbaugh, N. S. Flood size increases nonlinearly across the western United States in response to lower snow–precipitation ratios. *Water Resour. Res.* **56**, e2019WR025571 (2020).
7. Handwerger, A. L. et al. Widespread initiation, reactivation, and acceleration of landslides in the Northern California coast ranges due to extreme rainfall. *J. Geophys. Res. Earth Surf.* **124**, 1782–1797 (2019).
8. Haque, U. et al. The human cost of global warming: deadly landslides and their triggers (1995–2014). *Sci. Total Environ.* **682**, 673–684 (2019).
9. Martha, T. R. et al. Landslides triggered by the June 2013 extreme rainfall event in parts of Uttarakhand State, India. *Landslides* **12**, 135–146 (2014).
10. Morán-Ordóñez, A. et al. Future impact of climate extremes in the mediterranean: soil erosion projections when fire and extreme rainfall meet. *Land Degrad. Dev.* **31**, 3040–3054 (2020).
11. Nearing, M., Pruski, F. & O'neal, M. Expected climate change impacts on soil erosion rates: a review. *J. Soil Water Conserv.* **59**, 43–50 (2004).
12. Allen, M. R. & Ingram, W. J. Constraints on future changes in climate and the hydrologic cycle. *Nature* **419**, 228–232 (2002).
13. Trenberth, K. E. in *Weather and Climate Extremes* (eds Karl, T. R. et al.) 327–339 (Springer, 1999); https://doi.org/10.1007/978-94-015-9265-9_18.
14. Trenberth, K. E., Dai, A., Rasmussen, R. M. & Parsons, D. B. The changing character of precipitation. *Bull. Am. Meteorol. Soc.* **84**, 1205–1218 (2003).
15. Shi, X. & Durran, D. R. Estimating the response of extreme precipitation over midlatitude mountains to global warming. *J. Clim.* **28**, 4246–4262 (2015).
16. Diffenbaugh, N. S., Pal, J. S., Trapp, R. J. & Giorgi, F. Fine-scale processes regulate the response of extreme events to global climate change. *Proc. Natl Acad. Sci. USA* **102**, 15774–15778 (2005).
17. Räisänen, J. Warmer climate: less or more snow? *Clim. Dyn.* **30**, 307–319 (2007).
18. Krasting, J. P., Broccoli, A. J., Dixon, K. W. & Lanzante, J. R. Future changes in Northern Hemisphere snowfall. *J. Clim.* **26**, 7813–7828 (2013).
19. O'Gorman, P. A. Contrasting responses of mean and extreme snowfall to climate change. *Nature* **512**, 416–418 (2014).
20. Rhoades, A. M. et al. Asymmetric emergence of low-to-no snow in the midlatitudes of the American Cordillera. *Nat. Clim. Change* **12**, 1151–1159 (2022).
21. Siirila-Woodburn, E. et al. Evidence of a low-to-no snow future and its impacts on water resources in the western United States. *Nat. Revi. Earth Environ.* **2**, 800–819 (2021).
22. Kirschbaum, D. B., Stanley, T. & Simmons, J. A dynamic landslide hazard assessment system for Central America and Hispaniola. *Nat. Hazards Earth Syst. Sci.* **15**, 2257–2272 (2015).
23. Krøgli, I. K. et al. The Norwegian forecasting and warning service for rainfall- and snowmelt-induced landslides. *Nat. Hazards Earth Syst. Sci.* **18**, 1427–1450 (2018).
24. Oakley, N. S. A warming climate adds complexity to post-fire hydrologic hazard planning. *Earths Future* **9**, e2021EF002149 (2021).
25. Ombadi, M., Nguyen, P., Sorooshian, S. & Hsu, K.-l Developing intensity–duration–frequency (IDF) curves from satellite-based precipitation: methodology and evaluation. *Water Resour. Res.* **54**, 7752–7766 (2018).
26. Bonnin, G. et al. *NOAA Atlas 14 Precipitation-Frequency Atlas of the United States Volume 2 Version 3.0: Delaware, District of Columbia, Illinois, Indiana, Kentucky, Maryland, New Jersey, North Carolina, Ohio, Pennsylvania, South Carolina, Tennessee, Virginia, West Virginia* (NOAA, 2006); https://www.weather.gov/owp/hdsc_currentpf.
27. Hersbach, H. et al. The ERA5 global reanalysis. *Q. J. R. Meteorol. Soc.* **146**, 1999–2049 (2020).
28. Pepin, N. C. et al. Climate changes and their elevational patterns in the mountains of the world. *Rev. Geophys.* **60**, e2020RG000730 (2022).
29. Hausfather, Z., Marvel, K., Schmidt, G. A., Nielsen-Gammon, J. W. & Zelinka, M. Climate simulations: recognize the 'hot model' problem. *Nature* **605**, 26–29 (2022).
30. Sun, Q., Zhang, X., Zwiers, F., Westra, S. & Alexander, L. V. A global, continental, and regional analysis of changes in extreme precipitation. *J. Clim.* **34**, 243–258 (2021).
31. Pfahl, S., O'Gorman, P. A. & Fischer, E. M. Understanding the regional pattern of projected future changes in extreme precipitation. *Nat. Clim. Change* **7**, 423–427 (2017).
32. Marelle, L., Myhre, G., Hodnebrog, Ø., Sillmann, J. & Samset, B. H. The changing seasonality of extreme daily precipitation. *Geophys. Res. Lett.* **45**, 11–352 (2018).
33. Jennings, K. S., Winchell, T. S., Livneh, B. & Molotch, N. P. Spatial variation of the rain–snow temperature threshold across the Northern Hemisphere. *Nat. Commun.* **9**, 1148 (2018).
34. Risser, M. D. & Wehner, M. F. Attributable human-induced changes in the likelihood and magnitude of the observed extreme precipitation during hurricane Harvey. *Geophys. Res. Lett.* **44**, 12–457 (2017).
35. Paciorek, C. J., Stone, D. A. & Wehner, M. F. Quantifying statistical uncertainty in the attribution of human influence on severe weather. *Weather Clim Extrem.* **20**, 69–80 (2018).
36. Payne, A. E. et al. Responses and impacts of atmospheric rivers to climate change. *Nat. Rev. Earth Environ.* **1**, 143–157 (2020).
37. Immerzeel, W. W. et al. Importance and vulnerability of the world's water towers. *Nature* **577**, 364–369 (2019).
38. Milly, P. C. D. et al. Stationarity is dead: whither water management? *Science* **319**, 573–574 (2008).
39. Cheng, L. & AghaKouchak, A. Nonstationary precipitation intensity–duration–frequency curves for infrastructure design in a changing climate. *Sci. Rep.* **4**, 7093 (2014).
40. Ragno, E. et al. Quantifying changes in future intensity–duration–frequency curves using multimodel ensemble simulations. *Water Resour. Res.* **54**, 1751–1764 (2018).
41. Fowler, H. J. et al. Anthropogenic intensification of short-duration rainfall extremes. *Nat. Rev. Earth Environ.* **2**, 107–122 (2021).
42. Delaney, C. J. et al. Forecast informed reservoir operations using ensemble streamflow predictions for a multipurpose reservoir in Northern California. *Water Resour. Res.* **56**, 2019–026604 (2020).
43. O'Gorman, P. A. Precipitation extremes under climate change. *Curr. Clim. Change Rep.* **1**, 49–59 (2015).
44. Condom, T. et al. Climatological and hydrological observations for the South American Andes: in situ stations, satellite, and reanalysis data sets. *Front. Earth Sci.* **8**, 92 (2020).
45. Menne, M. J., Durre, I., Vose, R. S., Gleason, B. E. & Houston, T. G. An overview of the Global Historical Climatology Network-daily database. *J. Atmos. Ocean. Technol.* **29**, 897–910 (2012).
46. Xiong, W., Tang, G., Wang, T., Ma, Z. & Wan, W. Evaluation of IMERG and ERA5 precipitation-phase partitioning on the global scale. *Water* **14**, 1122 (2022).
47. Cartopy: A Cartographic Python Library with a Matplotlib Interface (Met Office, 2010–2015); https://scitools.org.uk/cartopy.

Methods

General selection of datasets

The selection of datasets for the analysis in the present study was carried out to satisfy five criteria: (1) the availability of estimates for both total and solid precipitation (precipitation and snowfall), from which rainfall estimates can be calculated; (2) a spatial resolution of at least 100 km to reasonably simulate orographic effects on precipitation, although a much higher resolution would ideally be needed to fully resolve orographic effects; (3) a fine temporal resolution to examine subdaily changes in rainfall extremes; (4) complete spatial coverage over the spatial domain of analysis (20° N–90° N); and (5) data covering the period 1950–2019. To our knowledge, ERA5[27], the fifth-generation atmospheric reanalysis of the global climate produced by the European Center for Medium-Range Weather Forecasts, is the only dataset that satisfied all of these criteria. It was, therefore, selected to analyse historical changes in rainfall extremes for the period 1990–2019 relative to the reference period 1950–1979. The ERA5 version used here, namely ERA5 hourly land data, combines model data with observations at a spatial resolution of 1° × 1° and hourly temporal resolution for the period 1950–2019. ERA5 has been shown to perform reasonably well for estimation of extreme precipitation[48] and snow–rain partitioning[46]. In this study, we provide an additional evaluation of ERA5 estimates of daily rainfall extremes against ground observations obtained from the GHCNd dataset. The evaluation results are shown in Extended Data Figs. 7 and 8 and discussed in 'Evaluation of ERA5 against ground observations'.

Similarly, the selection of CMIP6 model simulations was carried out to satisfy the aforementioned criteria. The main analysis presented in this study is carried out using future projections that assume the highest Shared Socioeconomic Pathways scenario associated with an increase of 8.5 W m^{-2} by the end of the year 2100, known as the SSP585 scenario. The selection of this high-emissions scenario is made because it is the worst-case scenario (known previously as the business-as-usual scenario); hence, it presents the most sharp and abrupt warming-induced perturbation in the climate system. We selected only Earth-system models with a nominal spatial resolution of 100 km or finer in our analysis (Extended Data Table 1). For each model, one ensemble member (r1i1p1f1) is selected. The eight selected models represent different institutions and reflect distinct modelling development backgrounds. All models apart from GFDL-ESM4 provide estimates of total precipitation and snow at a temporal resolution of 3 h, whereas only daily estimates are available for GFDL-ESM4. It is noteworthy that MRI-AGCM-3-2-H (nominal resolution of 60 km) is the model with the finest spatial resolution in the present study, and it belongs to the High-Resolution Model Intercomparison Project (HighResMIP)[49]. Unlike the fully coupled models (ocean + atmosphere) used in this study, MRI-AGCM-3-2-H is an Atmospheric Model Intercomparison Project (AMIP)-style experiment with prescribed sea surface temperature and ice conditions. Other HighResMIP models were not considered here owing to unavailability of snowfall estimates at subdaily to daily timescales. For each of the eight models, data were downloaded for precipitation (pr), snowfall (prsn), surface temperature (ts) and elevation (orog).

Selection of datasets to assess sensitivity to global warming levels

To account for differences in the models' warming sensitivity to emissions, we carried out an analysis of changes in rainfall extremes across four ensembles of model simulations corresponding to warming levels of +1.5 K, +2 K, +3 K and +4 K relative to the reference period (1950–1979). The model simulations used for each ensemble are listed in Extended Data Table 3. Overall, these simulations span 7 models and 4 emissions scenarios (ssp126, ssp245, ssp370 and ssp585), with each simulation representing a period of 30 years. It is noted that the HighResMIP model MRI-AGCM-3-2-H was not included in this analysis as it does not provide different simulations corresponding to different emissions like the other seven CMIP6 models. The 43 datasets were selected as follows: (1) a 30-year moving average of mean global surface temperature starting from the year 2018 was calculated for each simulation; (2) the difference between this moving average's mean surface temperature and that of the period 1950–1979 obtained from the same model was calculated; and (3) if a 30-year window has a temperature difference that lies within 0.1 K of the warming levels 1.5 K, 2 K, 3 K and 4 K, it was selected as an ensemble member for that specific warming level. This resulted in the datasets shown in Extended Data Table 3, which were then combined for each ensemble with equal weights.

Computation of percentage change in rainfall extremes

We first used total precipitation (p) and snowfall (s) estimates to generate rainfall (r) time series for each grid cell within each dataset as follows:

$$r_{i,j,t} = p_{i,j,t} - s_{i,j,t} \quad (1)$$

where the subscripts i, j and t correspond to the latitude, longitude and time step, respectively, for each variable. The output temporal frequency for the reanalysis dataset and CMIP6 model variables are 1 h and 3 h, respectively. Following this step, rainfall (r) is accumulated to duration (d) of 3 h, 12 h and 24 h. Next, the AMS were constructed by extracting the highest value of r in each year for all durations d as follows:

$$\mathrm{AMS}_{i,j,y} = \max_{t\in(\mathrm{year}=y)}\{r_{i,j,t}\} \quad (2)$$

where $\mathrm{AMS}_{i,j,y}$ is the AMS value for grid cell (i, j) and year y. The percentage change in rainfall extremes at each grid cell is then computed as the difference between the mean value of AMS for the future (or recent past) period minus that of the reference period (1950–1979) normalized by the mean AMS value of the reference period. For an arbitrary grid cell (i, j), let $\mathrm{AMS}_{\mathrm{ref}}$ denote the mean AMS for the reference period and $\mathrm{AMS}_{\mathrm{t}}$ denote the mean AMS for future (or recent past) period. Then, the percentage change at each grid cell is calculated as follows:

$$\%\mathrm{change} = [(\mathrm{AMS}_{\mathrm{t}} - \mathrm{AMS}_{\mathrm{ref}})/\mathrm{AMS}_{\mathrm{ref}}] \times 100\% \quad (3)$$

For the analysis of ERA5 historical changes, $\mathrm{AMS}_{\mathrm{t}}$ is computed from the period of 1990–2019, whereas the period 2071–2100 is used for CMIP6 models. The percentage changes are then divided by warming levels in global surface air temperature (Extended Data Table 2) to produce the results shown in Figs. 1–3. It is noted that the results for ERA5 in Fig. 1 show the mean percentage change at different elevation categories; however, similar results are obtained using the median instead of the mean. Extended Data Fig. 9 compares the use of mean and median to assess elevation-dependent amplification of rainfall extremes. Furthermore, to ensure that the results are not biased by issues related to the selection of reference period[50,51], we carried out a statistical simulation study similar to that of previous studies[50]. For each of 10,000 Monte Carlo replicates, we first generated 30 values from a 'baseline' period and 30 values from a 'future' period. Each set of values came from a known generalized extreme value (GEV) distribution (to mimic the appropriate distributions for AMS data). The specific scenarios considered for the distribution parameters are outlined in Extended Data Fig. 10b with one scenario where the distributions used to generate baseline and future data are identical such that the true percent change is zero. We then calculate the percent change from simulated data according to equation (3). For all simulations, the values of the GEV shape parameter were taken to be representative of those estimated from ERA5 data (for example, first quartile, median and so on). Extended Data Fig. 10a clearly shows that using 30 years as a reference period does not bias the results for values of shape parameter typical to ERA5 data and across change of 0% to 100%.

Masking out hyperarid regions

The %change calculations shown in equation (3) could be very sensitive in hyperarid regions where there is extremely low amount of rainfall (if any). These regions, such as parts of the Sahara Desert, can lead to extremely large and unrealistic values of %change that could be in the order of 1,000% to 10,000%. These values of change are highly susceptible to observational noise and they potentially bias the overall results. Therefore, in the spatial domain of our analysis (20° N–90° N), we masked out all regions that have mean annual rainfall of less than 20 mm in the reference period. Similarly, we have excluded regions that have mean AMS of daily rainfall less than 1 mm in the reference period. Regions with daily rainfall AMS of less than 1 mm are also susceptible to observational and estimation noise, which could lead to considerable biases. This procedure was performed separately for both ERA5 and each of the CMIP6 models. The regions masked out from the analysis are mostly located at subtropical parts of the Sahara Desert and Greenland (Extended Data Fig. 6). Both regions are primarily uninhabited and are therefore of limited interest to the analysis presented in this paper.

Re-gridding to a common spatial resolution

To assess changes in rainfall extremes in the multimodel mean (for example, Figs. 1 and 4 and Extended Data Fig. 1) and explore potential elevation-dependent increases in rainfall extremes (Fig. 1), all model data was resampled to a common spatial resolution of (1° × 1°). The re-sampling was carried out using bilinear interpolation. The elevation data used for this analysis are the Rand's global elevation dataset, which provides elevation data at 1° spatial resolution across the globe[52]. It should be noted that multimodel mean data were calculated using simple averaging with equal weights applied to all models. We examined the impact of re-sampling on the accuracy of the results by investigating the relationship between elevation and increases in rainfall at the native resolution of each model (shown in Extended Data Fig. 1c–e). Elevation files for each model were obtained from the CMIP6 repository for the variable 'orog'. The results are qualitatively and quantitatively indistinguishable from the ones with resampled data. Therefore, we conclude that the re-sampling approach used in this study had little to no impact on the results.

Regression of changes in rainfall extremes on elevation

To evaluate the relationship between elevation and the increase in rainfall extremes as shown in Fig. 1, we established a regression relationship over all grid cells within each model. For ERA5, we adopted a linear regression of the form $y = mx + b$, whereas third-order polynomial regression was adopted for CMIP6 models. Polynomial regression was used in the latter case because it improved the model fit unlike the case for ERA5 where the improvement was negligible. It should be noted that amplification patterns in CMIP6 models are evident even in the case of linear regression as shown in Extended Data Fig. 9a–c. It is also worthwhile to mention that all figures related to elevation-dependent amplification show the mean value of change in rainfall extremes at different elevation categories (black markers) and the 95% confidence interval (vertical lines). Those estimates are meant to show the general trend, which is not affected by the choice of the regression model.

Snow fraction of precipitation extremes

To quantify the change in snow fraction of precipitation extremes within each model and examine its impact on amplification of rainfall extremes, we started by extracting $AMS_{i,j,y}$ for all grid cells (i, j) within each dataset. The snow fraction of each event in the AMS is then calculated as the snowfall depth divided by total precipitation depth. This resulted in two time series for each grid cell corresponding to reference and future periods, each with 30 values of snow fraction. The mean of each time series is then computed and distributions of the values of snow fraction over all grid cells are then plotted as shown in Extended Data Fig. 2a. Moreover, the change in snow fraction for each grid cell is calculated as the difference between mean values of snow fraction for the reference and future period (future minus reference); these values are shown for each model in the horizontal axis of Extended Data Figs. 3 and 4. Finally, by averaging all values across grid cells, a single value of change in snow fraction for each model is estimated. These are the values shown in the horizontal axis of Fig. 3a.

Timing of precipitation extremes

For each grid cell (i, j) in a given dataset, the Julian day (1 to 366 corresponding to 1 January to 31 December) of $AMS_{i,j,y}$ was extracted for all years y in the reference and future period. This resulted in two time series, each of which has 30 values of Julian days, for the historical period (1950–1979) and the future period (2071–2100). Next, the circular mean of both time series was calculated to represent a single Julian day for the occurrence of precipitation extremes in each period. Finally, the absolute difference (future minus historical) was calculated to examine whether a seasonal shift in timing of extremes has occurred or not. The CDFs for all grid cells within each dataset were then plotted (Fig. 3c). Furthermore, an alternative approach in assessing the changes of timing in precipitation extremes using the modal month[53,54] was carried out. The results are shown in Extended Data Fig. 2b–i, and they are generally consistent with those in Fig. 3c, showing that most grid cells in all models have a change of timing that is less than 2 months. It is noted that all calculations related to the timing of precipitation extremes are carried out using total precipitation (liquid + solid). This is because our aim is to assess whether the timing of precipitation extremes has changed regardless of their composition (liquid versus solid).

Extreme-value analysis

Extreme-value analysis, or the study of rare events, is a branch of mathematical statistics that seeks to provide a formal framework for characterizing extremes and their uncertainty. The goal of extreme-value analysis is to quantify the magnitude or severity of a worst-case scenario, which often requires extrapolation to events that have not actually occurred. Extreme-value analysis does this by deriving theoretical results and formulas for how to properly carry out the extrapolation needed for a particular study. The AMS framework utilized in this paper lends itself to statistically modelling these data as arising from the GEV family of distributions. Extreme-value analysis theory (Theorem 3.1.1 on page 48 in ref. 55) shows that the CDF of the AMS can be approximated by a member of the GEV family

$$G(z) \equiv P(Z \le z) = \exp\{-[1 + \xi((z-\mu)/\sigma)]^{-1/\xi}\} \quad (4)$$

as the maxima arise from a large number of high-frequency measurements (daily, 12 h and so on) within a pre-specified time interval or 'block' (here, each year). In equation (4), Z denotes the AMS values for an arbitrary grid cell and each duration of interest from either the reference or future time period, and the CDF is defined for $\{z : 1 + \xi(z-\mu)/\sigma > 0\}$. The GEV family of distributions is characterized by three statistical parameters: μ, which describes the centre of the distribution; σ, which describes the spread or width of the distribution; and ξ, which is a unitless quantity that describes the upper-tail behaviour of the GEV distribution.

Although the statistical parameters of the GEV distribution are sometimes of direct interest, we are often more interested in summaries of the distribution, often referred to as return values, return probabilities and return periods. Return values (sometimes referred to as return levels) quantify an upper percentile of the GEV distribution, that is, a rainfall accumulation z such that the probability of exceeding z is small (for example, $P = 0.1$, $P = 0.05$ or $P = 0.01$). Return probabilities summarize the likelihood of exceeding a specified threshold, that is, the probability of exceeding a large rainfall accumulation. Return periods

are simply the inverse of the return probability and are used to quantify how often (on average) a particular threshold will be exceeded. The form of the GEV distribution allows us to write down formulas for each of these quantities based on $\{\mu, \sigma, \xi\}$ (see chapter 3 of ref. 55). For instance, the T-year return value, denoted $\emptyset(T)$, is

$$\emptyset(T) = \begin{cases} \mu - \frac{\sigma}{\xi}[1 - \{-\log(1-1/T)\}^{-\xi}], \xi \neq 0 \\ \mu - \sigma \log\left\{-\log\left(1-\frac{1}{T}\right)\right\}, \xi = 0 \end{cases} \quad (5)$$

such that the probability of exceeding $\emptyset(T)$ is $1/T$ (hence the 'T-year' terminology). The return probability for a pre-specified threshold z, denoted $\theta(z)$, is

$$\theta(z) = \begin{cases} 1 - \exp\left\{-\left[1 - \frac{\xi(\mu - z)}{\sigma}\right]^{-\frac{1}{\xi}}\right\}, \xi \neq 0 \\ 1 - \exp\{-\exp\{(\mu - z)/\sigma\}, \xi = 0 \end{cases} \quad (6)$$

and the return period is simply $1/\theta(z)$. Our analysis of the AMS data proceeds by first obtaining maximum likelihood estimates of the GEV parameters for each model grid cell and duration separately for the reference and future periods, denoted $\{\hat{\mu}_{\text{ref}}, \hat{\sigma}_{\text{ref}}, \hat{\xi}_{\text{ref}}\}$ and $\{\hat{\mu}_{\text{future}}, \hat{\sigma}_{\text{future}}, \hat{\xi}_{\text{future}}\}$ (here, the '$\hat{\cdot}$' denotes a statistical estimate of the true unknown parameter). These estimates can be plugged into equations (5) and (6) to obtain estimated return values and return probabilities (and, for that matter, return periods as well).

Finally, the risk ratio (RR) uses these formulae to quantify changes in the frequency of a pre-specified extreme event as follows: setting the threshold of interest to be the estimated T-year return value from the reference period (that is, $z = \hat{\emptyset}_{\text{ref}}(T)$), the RR in each grid cell and for each duration is

$$\text{RR}(T) = \frac{\hat{\theta}_{\text{future}}(\hat{\emptyset}_{\text{ref}}(T))}{\hat{\theta}_{\text{ref}}(\hat{\emptyset}_{\text{ref}}(T))} \quad (7)$$

where the estimated return value $\hat{\emptyset}_{\text{ref}}(T)$ is calculated as in equation (5) based on $\{\hat{\mu}_{\text{ref}}, \hat{\sigma}_{\text{ref}}, \hat{\xi}_{\text{ref}}\}$ and the estimated return probabilities $\hat{\theta}_{(\cdot)}(\cdot)$ are calculated as in equation (6). Two things should be noted in equation (7): first, the threshold of interest $\hat{\emptyset}_{\text{ref}}(T)$ is defined relative to the climatology of the grid cell of interest, so that the RR summarizes changes in the frequency of events that are considered 'extreme' for each geospatial location of interest. Second, the denominator of equation (7) is $1/T$, as the reference probability of exceeding the reference T-year return value is $1/T$ by definition.

Risk ratios for C–C only

To specifically quantify the effect of amplified rainfall extremes on the RR beyond what would be expected from C–C scaling (where we expect rainfall extremes to increase by approximately 7% K^{-1}), we can calculate a so-called C–C-only version of the RR as follows. It is noted that if a random variable X is distributed as GEV(μ, σ, ξ), the rescaled kX is distributed as GEV($k\mu, k\sigma, \xi$). Following from equation (7), we can define a C–C-only RR as

$$\text{RR}_{\text{CC-only}}(TT) = \frac{\hat{\theta}_{\text{CC-only}}(\hat{\emptyset}_{\text{ref}}(T))}{\hat{\theta}_{\text{ref}}(\hat{\emptyset}_{\text{ref}}(T))} \quad (8)$$

where $\{\hat{\mu}_{\text{CC-only}}, \hat{\sigma}_{\text{CC-only}}, \hat{\xi}_{\text{CC-only}}\} = \{k\hat{\mu}_{\text{ref}}, k\hat{\sigma}_{\text{ref}}, k\hat{\xi}_{\text{ref}}\}$. The value of k is model-specific and set equal to $1 + 0.07W$, where W is the degrees of warming from the reference period to future period in each model. We can then summarize both the 'actual' risk ratios RR(T) as well as the ratio of risk ratios RR(T)/$RR_{\text{CC-only}}(T)$, which quantifies the multiplicative change to the risk of rainfall extremes beyond what would be expected from C–C-scaling only.

Welch's t-test

We used Welch's t-test[56] in this study to assess whether the difference between the mean of two groups is statistically significant or whether it could be simply due to chance. The test is applied in cases where the two groups differ in their sample size (n_1 and n_2) and their variance (var_1 and var_2). The test is based on the assumption that the samples in the two groups are normally distributed. The t-statistic is calculated as follows:

$$t = \frac{\overline{X_1} - \overline{X_2}}{\sqrt{\frac{\text{var}_1}{n_1} + \frac{\text{var}_2}{n_2}}} \quad (9)$$

where $\overline{X_1}$ and $\overline{X_2}$ are the means of the samples in the two groups.

Evaluation of ERA5 against ground observations

We carried out an evaluation of ERA5 AMS of daily rainfall against observational in situ datasets. The evaluation was conducted in two approaches using the GHCNd dataset[45]. The first approach, hereafter referred to as analysis 1, is based on stations that have observations of both total-phase precipitation (p) and snowfall (s). We then calculate rainfall estimates as the difference ($p - s$) following equation (1). Overall, there is a total of 13,194 stations in the spatial domain 20° N–90° N with at least 20 years of observations after excluding years with more than 10% of missing daily observations. These stations, shown in Extended Data Fig. 7a, are mostly located in North America and they are used for analysis 1. The second approach, hereafter referred to as analysis 2, is based on stations that have observations of both precipitation and temperature. In this approach, daily mean temperature is used to partition p estimates into solid and liquid forms using a temperature-based scheme for rain–snow partitioning. The scheme we used here is adopted from refs. 19,57, and it simply approximates the snow fraction by the relationship $\exp(0.0000858(T + 7.5)^{4.12})$ where T is daily mean surface air temperature in units of °C for values in the range of −4 °C and 7 °C. In addition, for temperature values below −4 °C, all p is assumed to be snowfall, whereas for values above 7 °C, all p is assumed to be rainfall. For analysis 2, there is a total of 20,349 stations in the spatial domain 20° N–90° N with many stations located outside North America (Extended Data Fig. 7b).

The evaluation was carried out as follows. First, AMS of daily rainfall for GHCNd was constructed for both reference and recent past periods. Second, AMS of daily rainfall obtained from ERA5 was interpolated to the location of the GHCNd stations using bilinear interpolation. Third, the relative error (RE) in estimates of ERA5 daily rainfall extremes was calculated as follows:

$$\text{RE} = ((\text{AMS}_{\text{GHCNd}} - \text{AMS}_{\text{ERA5}})/\text{AMS}_{\text{GHCNd}}) \times 100\% \quad (10)$$

where $\text{AMS}_{\text{GHCNd}}$ and AMS_{ERA5} are the mean AMS of daily rainfall obtained from GHCNd and ERA5, respectively. The above equation is applied to all stations for both the reference period 1950–1979 and the recent past period 1990–2019. Extended Data Fig. 8a–d shows the distribution of RE for all stations in analysis 1. In Extended Data Fig. 8a,c, it is clear that 60% to 69% of all stations have an RE in the range of −20% to 30%, which is quite reasonable given the uncertainties associated with measurements of snowfall such as under-catch issues[58–60]. Furthermore, Extended Data Fig. 8b,d shows the REs at stations grouped by mean winter temperature and clearly demonstrates that ERA5 is more adequate in estimating extreme rainfall over cold regions, which is of importance to the analysis presented in this study.

The results for analysis 2, shown in Extended Data Fig. 8e–h, are qualitatively similar to those of analysis 1 albeit with a lower percentage stations (50%) having REs within the range −20% to 30%. However, one must

recognize that the data used in analysis 2 have additional uncertainty owing to the fact that liquid and solid phases of precipitation were estimated using the temperature-based scheme described above (as opposed to directly observed such as in analysis 1). It should be noted that the histograms (grey colour) for both analysis 1 and analysis 2 across all periods are centred at about 10% to 15% of RE, which means that ERA5 is systematically underestimating the values of extreme rainfall compared with observations. This means that a major component of the errors is a systematic error (as opposed to random error). This systematic error is commonly found when assessing gridded data against point data[25], which is attributed to the spatial averaging of precipitation fields over grid cells. The fact that the distributions for both reference and recent past periods are qualitatively similar (location, scale and general shape of the distribution) suggests that the systematic error component is consistent for both reference and recent past periods, which can be clearly seen from the plots in Extended Data Fig. 8i,j. For both analysis 1 and 2, 51% to 57% of the stations have REs in reference and recent past periods that lie within ±10% of each other. This type of systematic error cancels out when comparing recent past to reference periods and therefore is less likely to bias the results.

Amplification patterns in observational dataset

We carried out an investigation of amplification patterns in rainfall extremes as a function of elevation, which is shown in Extended Data Fig. 7c,d for analysis 1 and analysis 2, respectively. The results show that there is a clear amplification pattern in the percentage change of rainfall extremes for analysis 2 (Extended Data Fig. 7d) with both mean values of change at different elevation categories (black markers and vertical lines) and regression line fitted to all data points (black line and shading) showing an increase with elevation. The results are less clear with regard to analysis 1 (Extended Data Fig. 7c) where the mean values of change at different elevation categories do not show an amplification; however, the regression line fitted to all data points show an amplification pattern. Although these results provide an additional line of evidence to the amplification patterns observed in ERA5 and the CMIP6 models, one must acknowledge the uncertainties of these results, especially owing to the non-uniform sampling of stations within different elevation ranges (as shown in the maps of Extended Data Fig. 7a,b). In addition, it is clear that the stations used in analysis 1 and analysis 2 do not cover the same range of elevation bands covered by ERA5 and the CMIP6 models. For instance, the stations in analysis 1 cover an elevation range of 0 to 4,750 m. The lack of amplification patterns for the means at elevation categories in Extended Data Fig. 7c can be attributed to the non-uniformity of spatial distribution of stations in analysis 1 and their limited spatial domain covering only North America.

Data availability

CMIP6 data of the eight models used in this study are available from the Program for Climate Model Diagnosis and Intercomparison (PCMDI) at https://esgf-node.llnl.gov/projects/cmip6/. ERA5 hourly land data are available from the Copernicus Climate Change Service (C3S) Climate Date Store at https://cds.climate.copernicus.eu/cdsapp#!/dataset/reanalysis-era5-land?tab=overview. Rand's Global Elevation dataset is available from the Research Data Archive (RDA) at the National Center for Atmospheric Research (NCAR) at https://rda.ucar.edu/datasets/ds750.1/.

Code availability

The code and supporting data used in this analysis are available at https://doi.org/10.5281/zenodo.7740037 with GitHub access through https://doi.org/10.5281/zenodo.7796633.

48. Mahto, S. S. & Mishra, V. Does ERA-5 outperform other reanalysis products for hydrologic applications in India? *J. Geophys. Res. Atmos.* **124**, 9423–9441 (2019).
49. Haarsma, R. J. et al. High resolution model intercomparison project (HighResMIP v1.0) for CMIP6. *Geosci. Model Dev.* **9**, 4185–4208 (2016).
50. Sippel, S. et al. Quantifying changes in climate variability and extremes: pitfalls and their overcoming. *Geophys. Res. Lett.* **42**, 9990–9998 (2015).
51. Donat, M. G., Lowry, A. L., Alexander, L. V., O'Gorman, P. A. & Maher, N. Addendum: More extreme precipitation in the world's dry and wet regions. *Nat. Clim. Change* **7**, 154–158 (2017).
52. *Rand's Global Elevation and Depth Data. Research Data Archive at the National Center for Atmospheric Research, Computational and Information Systems Laboratory, Boulder CO* (RAND Corporation, 1980); https://doi.org/10.5065/HKKR-P122.
53. Barbero, R. et al. A synthesis of hourly and daily precipitation extremes in different climatic regions. *Weather Clim. Extrem.* **26**, 100219 (2019).
54. Fowler, H. J. & Kilsby, C. G. Implications of changes in seasonal and annual extreme rainfall. *Geophys. Res. Lett.* **30**, 1720 (2003).
55. Coles, S. *An Introduction to Statistical Modeling of Extreme Values* (Springer, 2001); https://doi.org/10.1007/978-1-4471-3675-0.
56. Welch, B. L. The generalization of "Student's" problem when several different population variances are involved. *Biometrika* **34**, 28–35 (1947).
57. Feiccabrino, J., Gustafsson, D. & Lundberg, A. Surface-based precipitation phase determination methods in hydrological models. *Hydrol. Res.* **44**, 44–57 (2012).
58. Yang, D. et al. Wind-induced precipitation undercatch of the Hellmann gauges. *Hydrol. Res.* **30**, 57–80 (1999).
59. Wolff, M. A. et al. Derivation of a new continuous adjustment function for correcting wind-induced loss of solid precipitation: results of a Norwegian field study. *Hydrol. Earth Syst. Sci.* **19**, 951–967 (2015).
60. Kochendorfer, J. et al. Undercatch adjustments for tipping-bucket gauge measurements of solid precipitation. *J. Hydrometeorol.* **21**, 1193–1205 (2020).
61. Kelso, N. V. & Patterson, T. *World Land-Based Polygon Features, 1:10 Million* (North American Cartographic Information Society, 2012); http://www.naturalearthdata.com.

Acknowledgements This research was supported by Office of Science, Office of Biological and Environmental Research of the US Department of Energy under contract no. DE-AC02-05CH11231 for the CASCADE Scientific Focus (funded by the Regional and Global Model Analysis Program area within the Earth and Environmental Systems Modeling Program) and the iNAIADS Early Career Research Project (funded by the Environmental Systems Science programme).

Author contributions M.O. devised the idea, designed the study, processed the data, performed the analysis, prepared figures and tables, and drafted the paper. M.D.R. performed the extreme-value analysis and contributed to the review and editing of the paper. A.R. contributed to the review and editing of the paper and provided subject-specific expertise in mountain hydroclimatology. C.V. contributed to the review and editing of the paper. Both M.R. and C.V. acquired funding for this research work.

Competing interests The authors declare no competing interests.

Additional information

Supplementary information The online version contains supplementary material available at https://doi.org/10.1038/s41586-023-06092-7.

Correspondence and requests for materials should be addressed to Mohammed Ombadi.

Peer review information *Nature* thanks Hayley Fowler and the other, anonymous, reviewer(s) for their contribution to the peer review of this work. Peer reviewer reports are available.

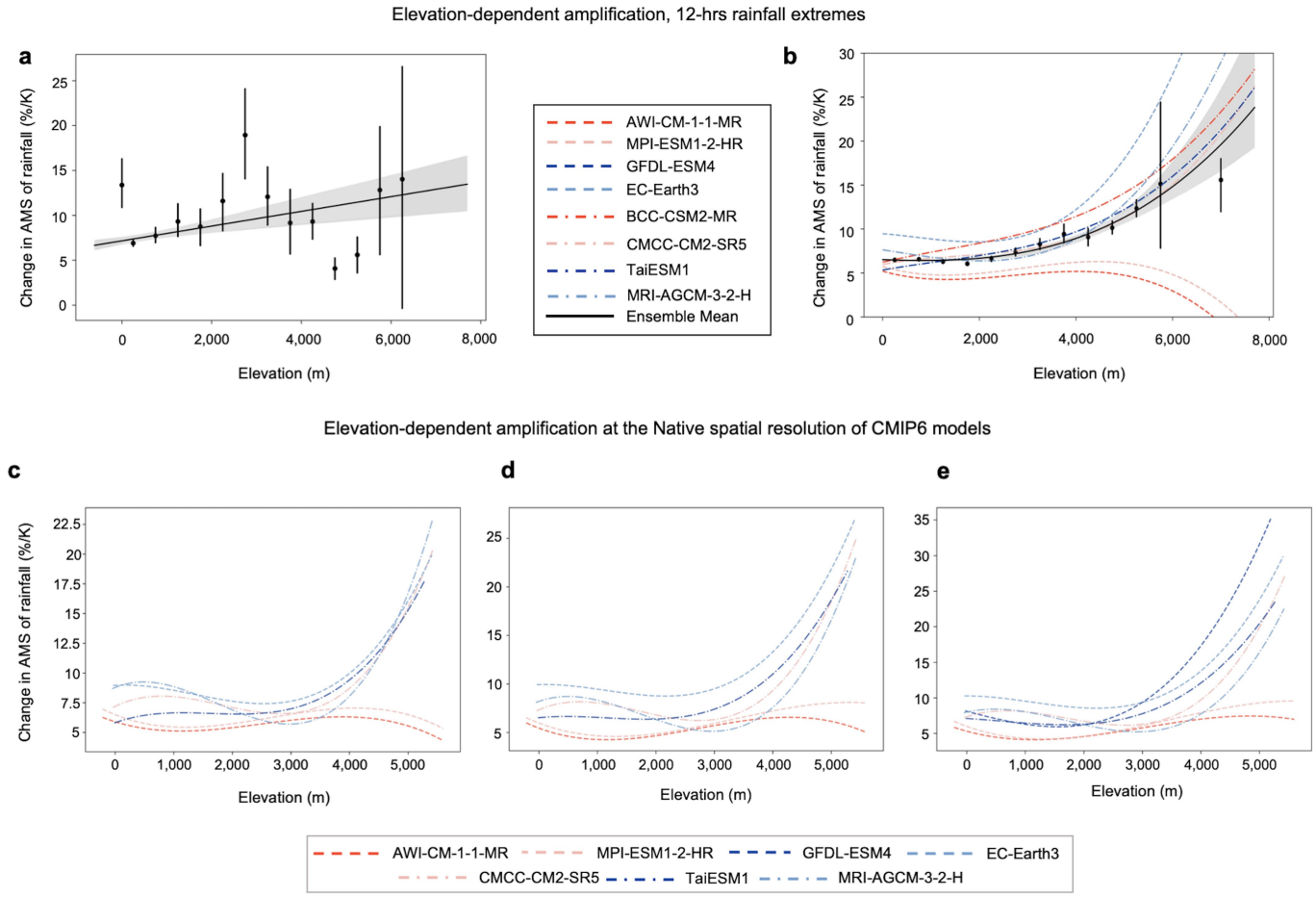

Extended Data Fig. 1 | Elevation-dependent amplification of rainfall extremes. All panels in the figure show percentage change in rainfall extremes, normalized by degrees of warming and expressed as a function of elevation over the spatial domain (20° N–90° N) land area with masking of hyper-arid regions (Methods). **a**, ERA5 12-hours annual maximum series (AMS) of rainfall. **b**, CMIP6 models (colored dashed and dash-dotted lines) and their multi-model mean (solid black line) for 12-hours AMS of rainfall. **c,d,e**, Percentage change in rainfall extremes at the native spatial resolution of the models (as opposed to resampled data). Note that the model BCC-CSM2-MR is not included because of missing elevation files in the CMIP6 repository. In all panels, regression is based on all grid cells within the spatial domain (not shown in the figure). For panels a and b, black markers and error bars indicate the mean percentage change at different elevation categories and its 90% confidence interval for ERA5 and CMIP6 multi-model mean. The shaded area surrounding regression lines in panels a and b represents the 95% confidence interval of regression estimates. Note that vertical axes in panels have different range of values.

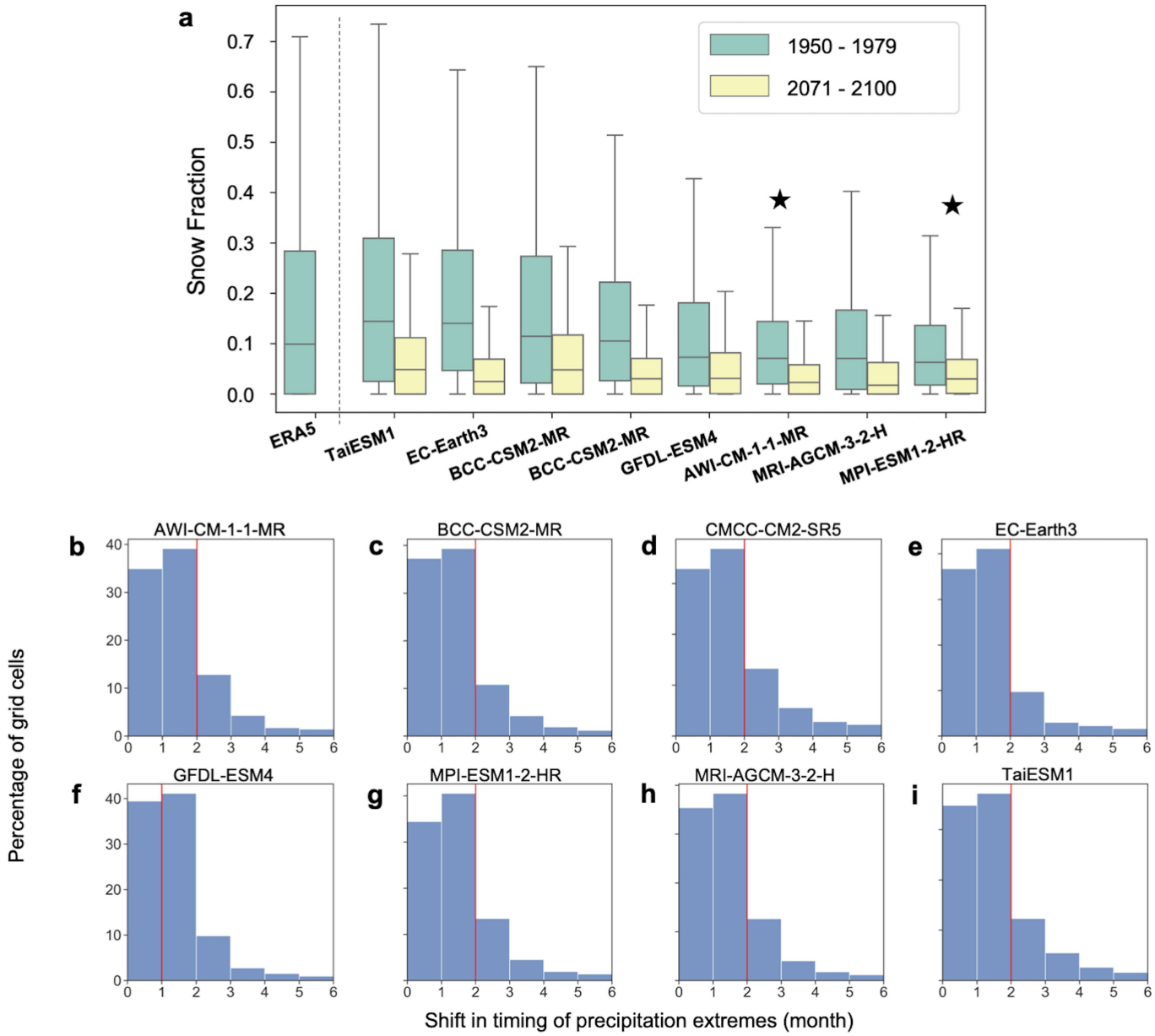

Extended Data Fig. 2 | Changes in snow fraction and timing of precipitation extremes. a, Snow fraction in annual maximum series (AMS) of daily precipitation for all grid cells in the spatial domain of (20° N–90° N) within ERA5 and CMIP6 models. Dark and light green boxplots correspond to the reference period (1950–1979) and the future period (2071–2100), respectively. The two models of AWI-CM-1-1-MR and MPI-ESM1-2-HR are highlighted with an asterisk due to their peculiar patterns of lacking amplification in rainfall extremes at high elevations. The boxes show the interquartile range (IQR; 75th percentile – 25th percentile) while the whiskers show the extent of the distribution, excluding outliers defined as values greater than (75th percentile + 1.5*IQR) or lower than (25th percentile – 1.5*IQR). **b–i**, Histograms summarize the shift in timing of precipitation extremes across the eight CMIP6 models used in the present study. Each histogram shows the shift in the modal month of precipitation extremes in the future period (2071–2100) compared to the baseline period (1950–1979) across grid cells within the spatial domain of (20° N–90° N). Red vertical lines represent the 80th percentile of timing shift in the modal month.

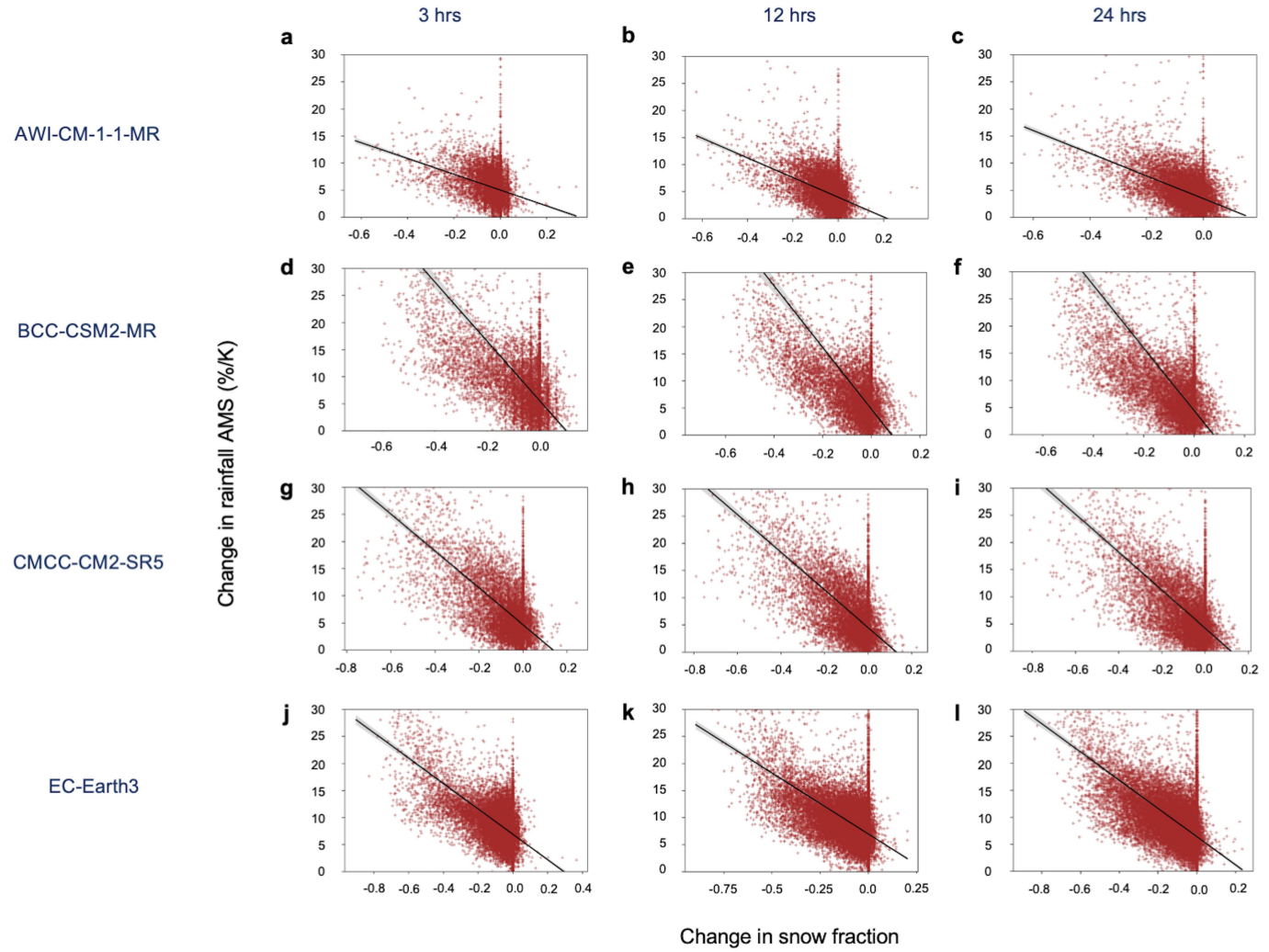

Extended Data Fig. 3 | Reduction in snow fraction amplifies rainfall extremes. **a**–**c**, Scatter plots for the relationship between change in snow fraction (horizontal axis) and percentage change in rainfall extremes (vertical axis) for CMIP6 model AWI-CM-1-1-MR, and rainfall duration of 3, 12- and 24-hours, respectively. Red markers represent individual grid cells whereas black line and shaded area represent least-squares linear regression fit and its 95% confidence interval, respectively. **d**–**f**, Same as a-c but for BCC-CSM2-MR. **g**–**i**, Same as a-c but for CMCC-CM2-SR5. **j**–**l**, Same as a-c but for EC-Earth3. In all panels, the changes in snow fraction and rainfall extremes are computed for the period (2071–2100) relative to the baseline period (1950–1979) for grid cells within the spatial domain of (20° N–90° N) land area with masking of hyper-arid regions (Methods).

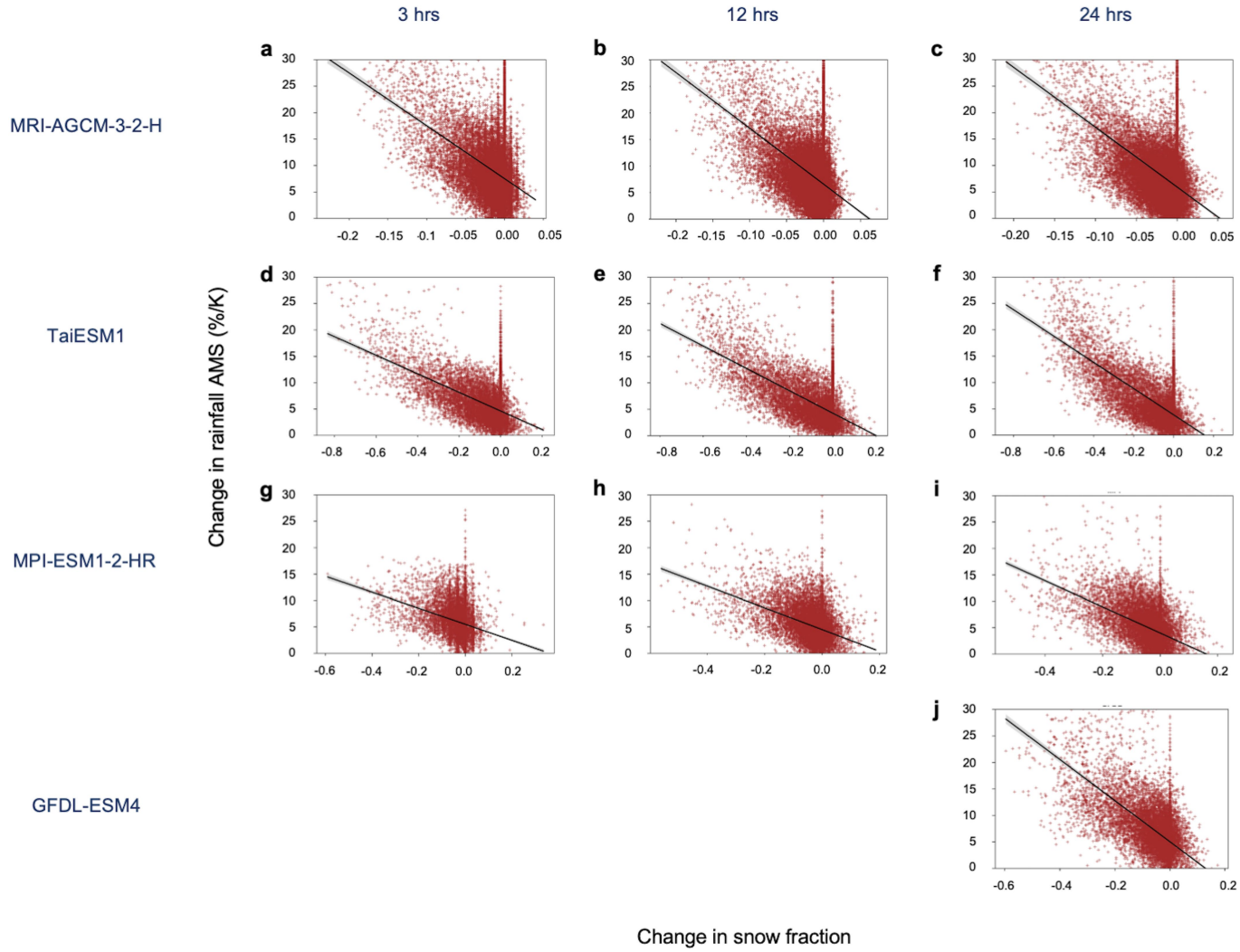

Extended Data Fig. 4 | Reduction in snow fraction amplifies rainfall extremes. **a**–**c**, Scatter plots for the relationship between change in snow fraction (horizontal axis) and percentage change in rainfall extremes (vertical axis) for CMIP6 model MRI-AGCM-3-2-H, and rainfall duration of 3-, 12- and 24-hours, respectively. Red markers represent individual grid cells whereas black line and shaded area represent least-squares linear regression fit and its 95% confidence interval, respectively. **d**–**f**, Same as a-c but for TaiESM1. **g**–**i**, Same as a- c but for MPI-ESM1-2-HR. **j**, Same as a but for GFDL-ESM4. Note that 3- and 12-hours results for the model GFDL-ESM4 are not shown because only daily temporal resolution was available for this model. In all panels, the changes in snow fraction and rainfall extremes are computed for the period (2071–2100) relative to the baseline period (1950–1979) for grid cells within the spatial domain of (20° N–90° N) land area with masking of hyper-arid regions (Methods).

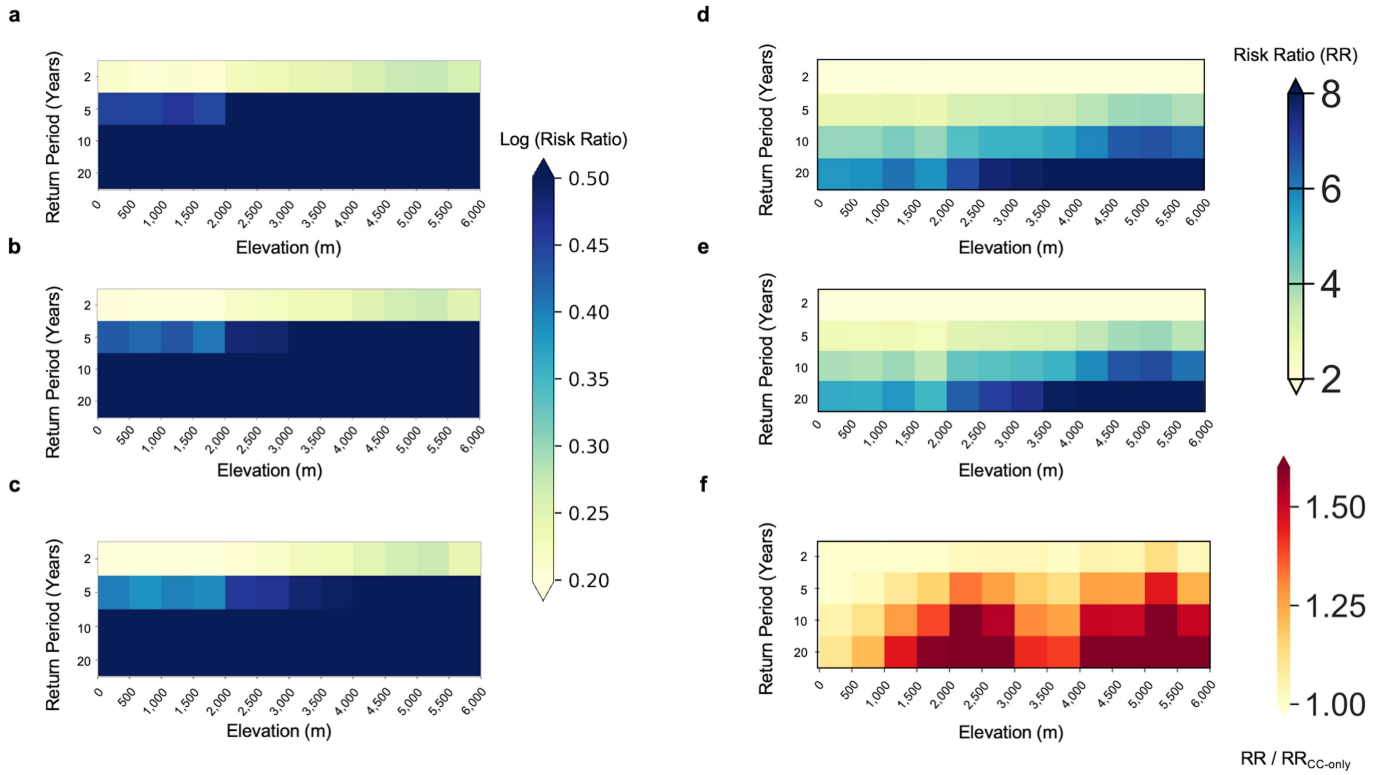

Extended Data Fig. 5 | Projected risk of rainfall extremes. a,b,c, A heatmap of Log_{10} (Risk Ratio) estimated from a multi-model mean of CMIP6 projections for the period (2071–2100) compared to baseline period (1950–1979). Estimates are averaged for grid cells within each elevation category (e.g., 0–500 m, 500–1,000 m ... 5,500–6,000 m) for rainfall duration of 3-, 12- and 24-hours, respectively. The vertical axis in a,b,c corresponds to T-year return values for T = 2, 5, 10, 20 years. **d,e**, Same as a,b,c but for the actual values of Risk Ratio (*RR*) for 3- and 12-hours rainfall, respectively. **f**, The ratio of risk ratios $RR/RR_{CC-only}$ quantifies the multiplicative change in risk estimated from the multi-model mean projections compared to the risk expected from Clausius-Clapeyron scaling. Results in panel f are shown for 24 hours rainfall.

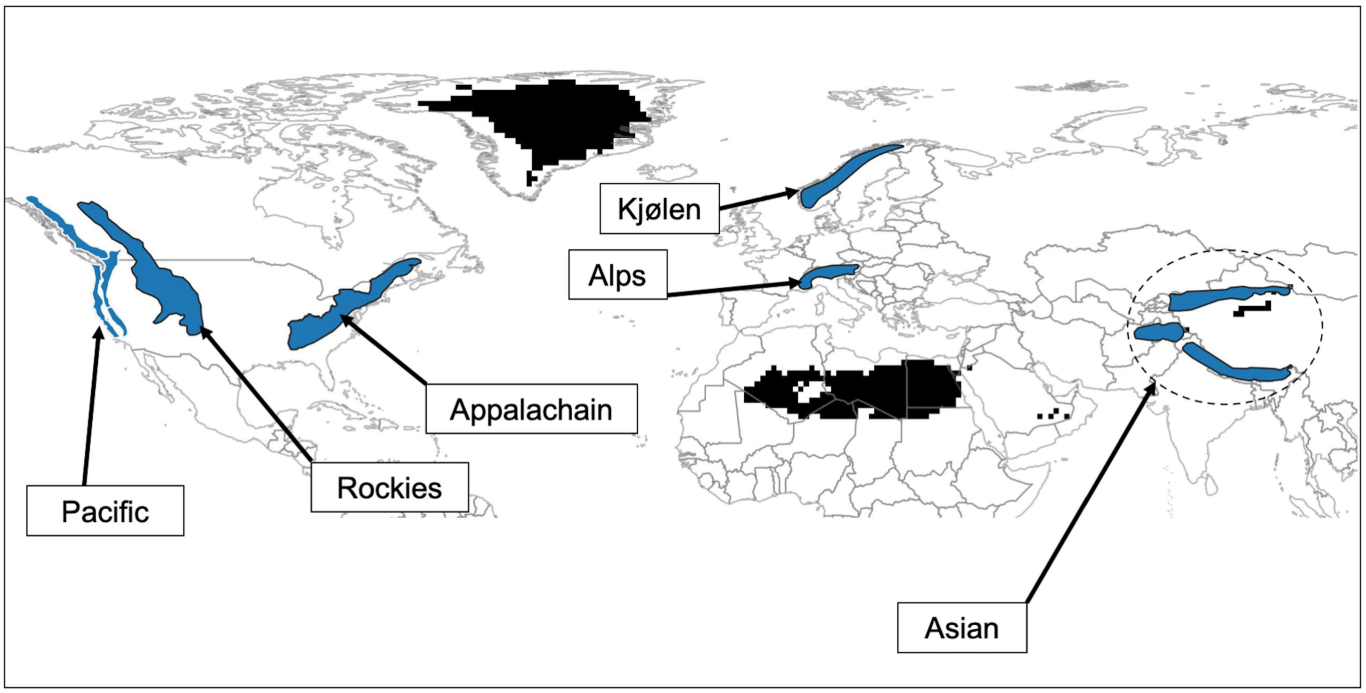

Extended Data Fig. 6 | Mountainous and hyper-arid regions. The spatial extent of the six mountain ranges used to investigate changes in Risk Ratio (RR) is shown in blue color. The six mountain ranges are: North American Pacific (Pacific), Rockies, Appalachian, Kjølen, Alps and Asian mountain ranges. The Asian ranges consist of the Himalayas, Tian Shan and Hindu Kush mountains. Regions in black shading are hyper-arid regions excluded from analysis (see Methods for details). Continental Map with boundaries of countries is obtained from Esri ArcGIS World Countries (Generalized) shapefiles, whereas the spatial extent of mountainous regions is obtained from the World Land-Based Polygon Features[61].

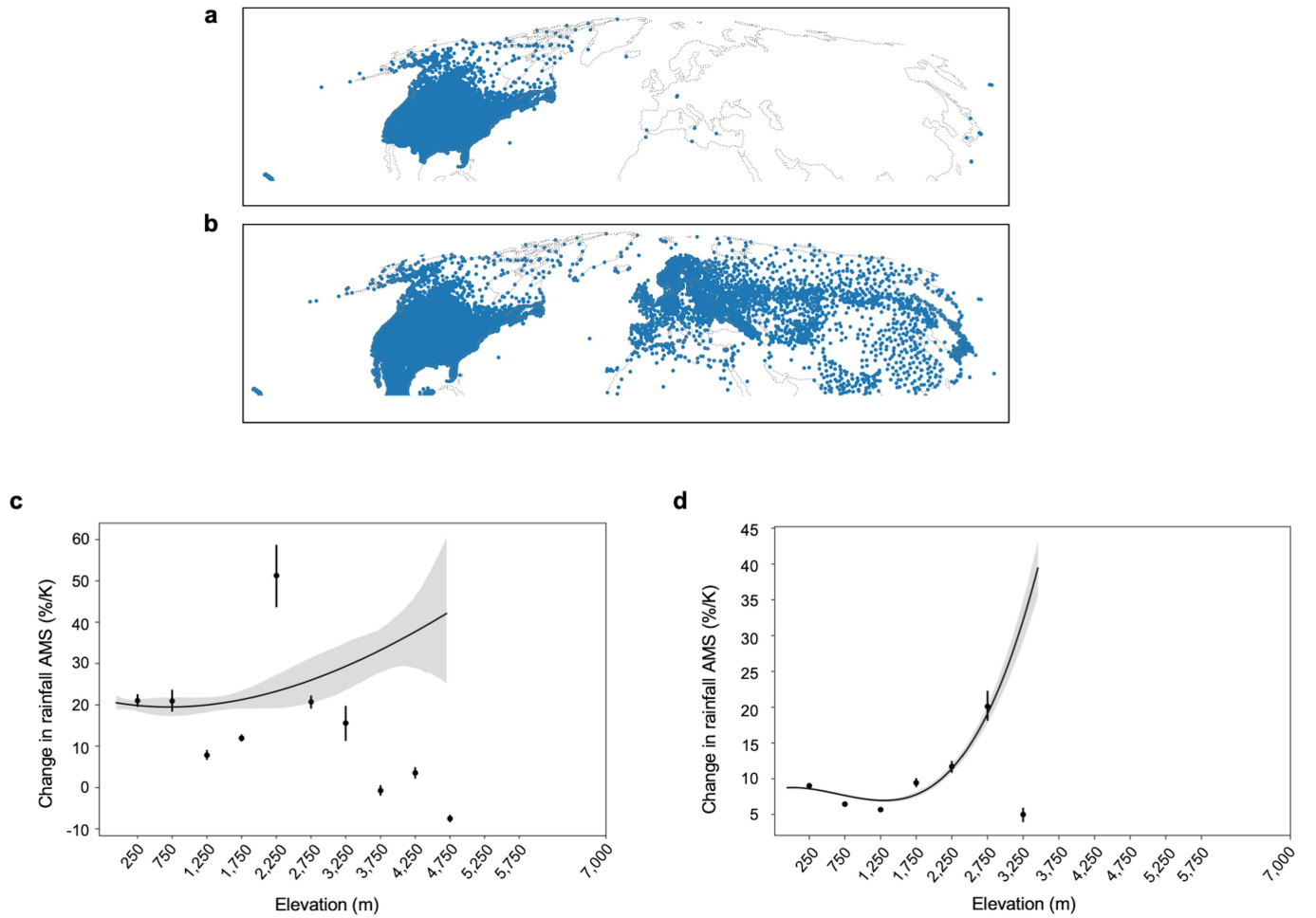

Extended Data Fig. 7 | Elevation-dependent amplification of rainfall extremes in observations. a, Stations from the Global Historical Climatology Network daily (GHCNd) data set used in analysis 1 are shown in blue markers. Total number of stations (n = 13,194) which have measurements of both precipitation and snowfall. **b**, Stations from GHCNd used in analysis 2 are shown in blue markers. Total number of stations (n = 20,349) which have measurements of both precipitation and daily mean temperature. **c**, The percentage change in daily rainfall extremes as a function of elevation for the period (1990–2019) compared to that of (1950–1979) for GHCNd stations in analysis 1. **d**, Same as c but for GHCNd stations in analysis 2. For panels c and d, regression is based on all stations within each analysis (not shown in the figure), and the shaded area surrounding regression line represents the 95% confidence interval. Additionally, black markers and error bars indicate the mean percentage change at different elevation categories and its 90% confidence interval, respectively. Maps in panels a,b were generated using Cartopy[47].

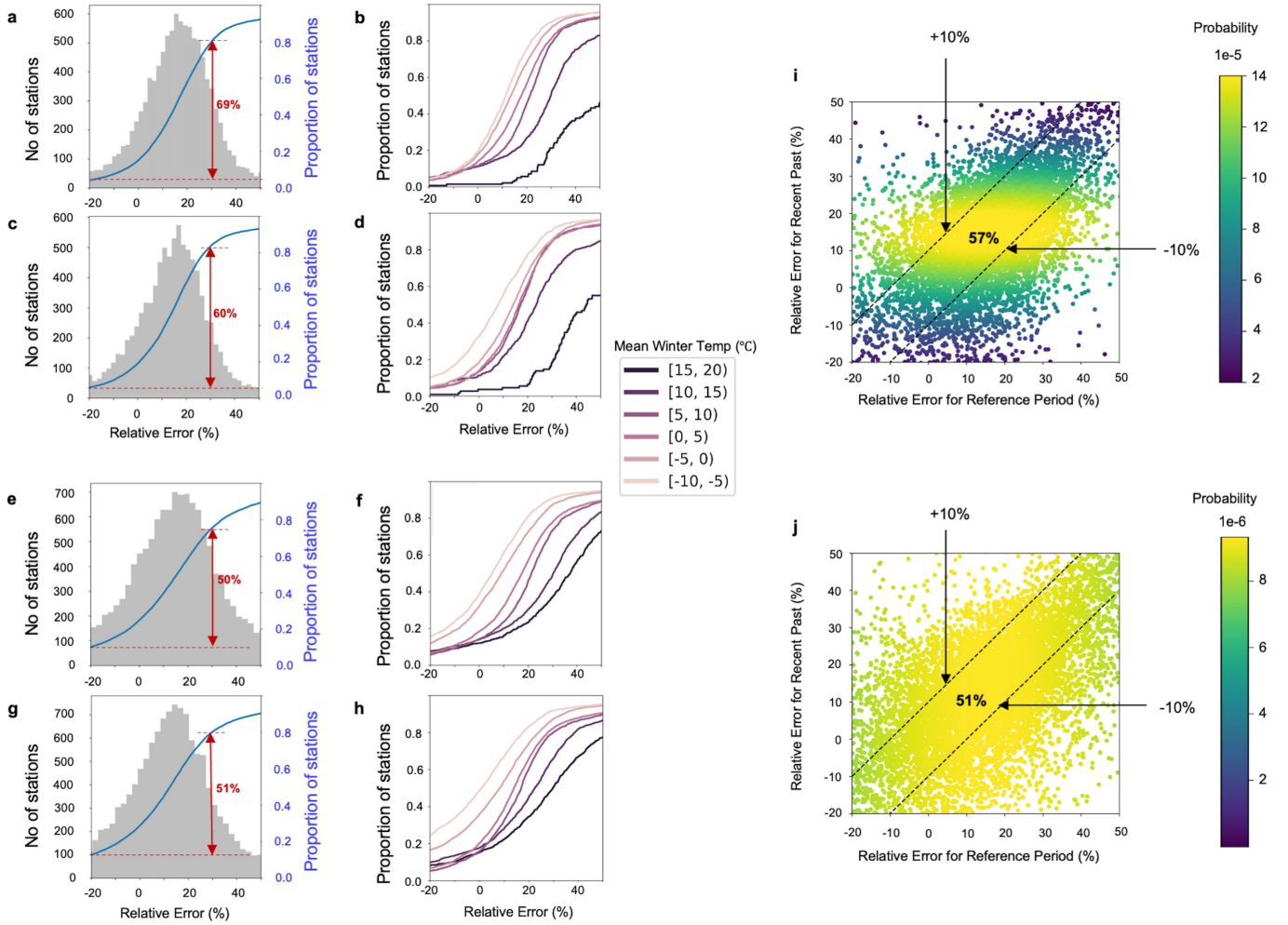

Extended Data Fig. 8 | Evaluation of ERA5 against ground observations. **a**, Histogram in gray color summarizes the relative error in the estimates of ERA5 daily rainfall extremes relative to observations in GHCNd stations of analysis 1 for the baseline period (1950–1979). Cumulative distribution function (cdf) is also shown in blue color. **c**, Same as a but for the recent past period (1990–2019). **b**, cdf of average relative error for analysis 1 stations categorized into distinct classes of mean Winter temperature in units of °C for the baseline period (1950–2019). **d**, Same as b but for the recent past period (1990–2019). **e**–**h**, Same as panels a-d but for analysis 2. For panels a,c,e,g, the red arrow and text show the percentage of stations that have relative error values in the range of −20% to 30%. **i**,**j**, Scatter plots for the relationship between the relative error of the reference period (horizontal axis) and recent past period (vertical axis) for GHCNd stations in analysis 1 and analysis 2, respectively. For panels i,j, the dotted lines indicate the range of (−10% to +10%) with the percentage of stations falling within the range shown in black text. Additionally, the scatter plots are visualized as density plots to clearly indicate the density of points.

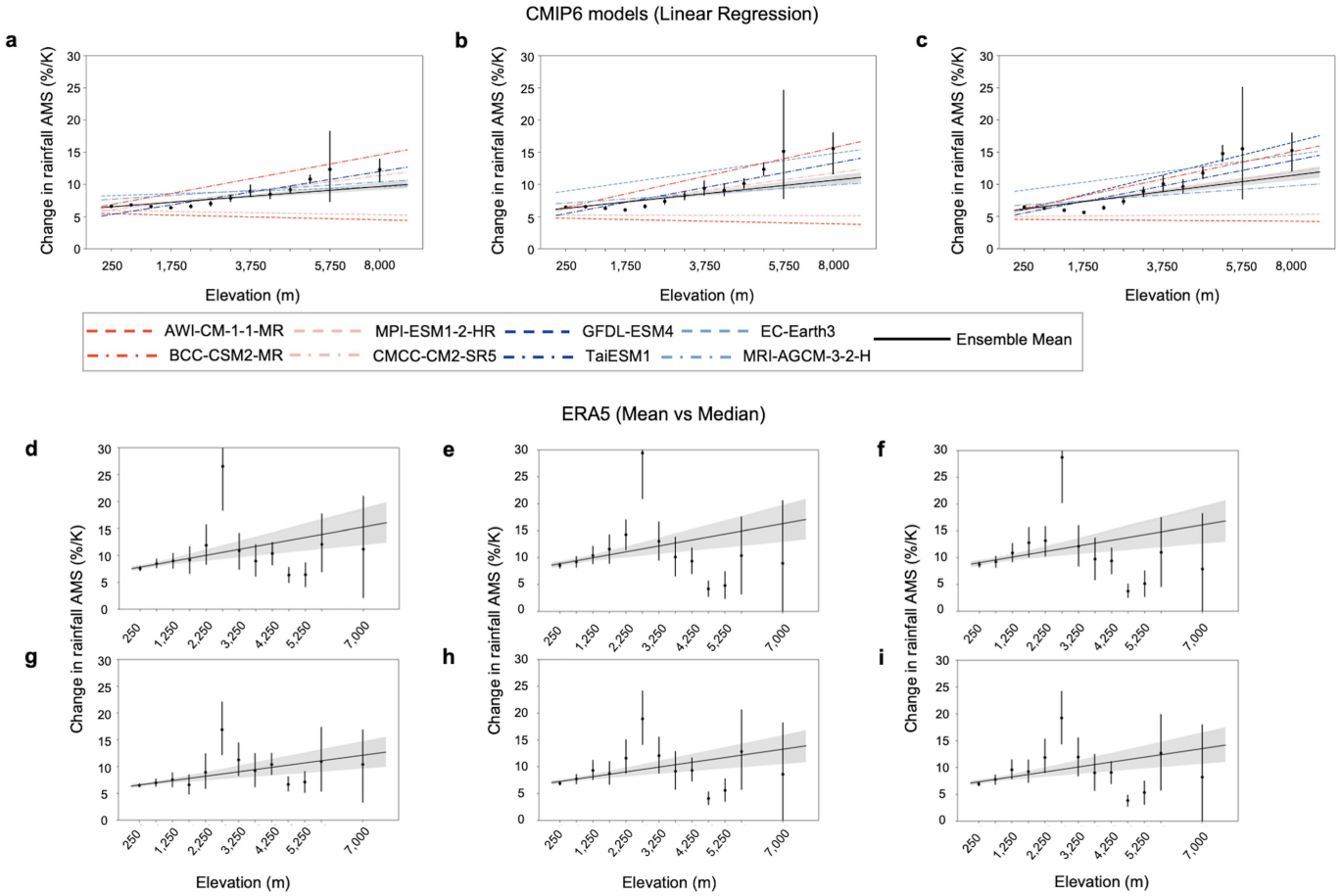

Extended Data Fig. 9 | Elevation-dependent amplification of rainfall extremes. a–**c**, Percentage change in rainfall extremes, normalized by degrees of warming, and expressed as a function of elevation over the spatial domain (20° N–90° N) land area with masking of hyper-arid regions (Methods) for rainfall duration of 3-, 12- and 24-hours, respectively. Colored dashed and dash-dotted lines and solid black line show least squares linear regression fit for eight CMIP6 models and their multi-model mean, respectively. Black markers and error bars show the mean percentage change at distinct elevation categories and its 90% confidence interval. **d**–**f**, Percentage change in rainfall extremes as a function of elevation for ERA5 data set with black markers and error bars showing mean percentage change at different elevation categories and its 90% confidence interval. **g**–**i**, Same as d-f but using median instead of mean. For panels d-f, black line shows the least-squares linear regression fit for all grid cells (not shown in the figure). For all panels, shading indicates the 95% confidence interval of regression fit.

a

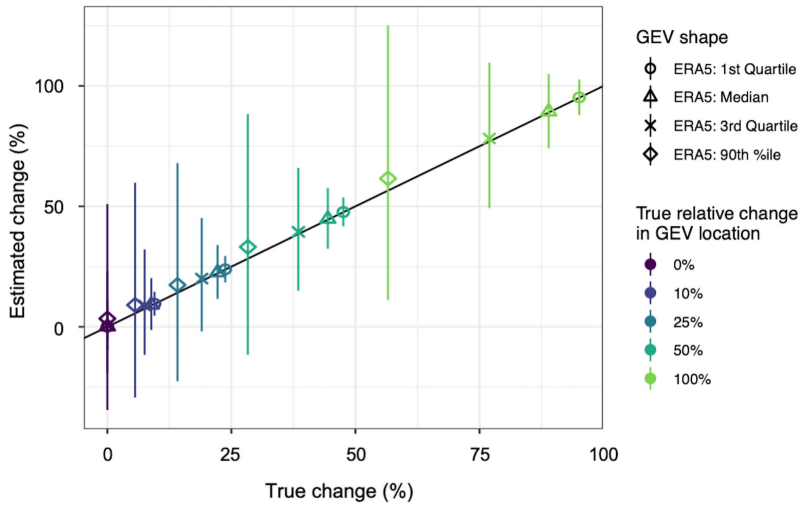

b

Baseline GEV location parameter	Future GEV location parameter	True relative change in GEV location
10	10	0%
10	11	10%
10	12.5	25%
10	15	50%
10	20	100%

Extended Data Fig. 10 | Robustness of results to selection of reference period. a, Results of a statistical simulation study with 10,000 Monte Carlo replicates drawn from two generalized extreme value (GEV) distributions for reference and future period. The horizontal axis shows the true percent change, whereas the vertical axis shows the percent change estimated from simulations. The markers and vertical bars show the mean change and its 90% confidence interval across the Monte Carlo replicates. Markers correspond to different values of shape parameter typical to those estimated from ERA5 data (e.g., 1st quartile, median). **b**, The table shows the values of location parameter for both baseline and future GEV and the corresponding percent change for the different simulations in this study.

Extended Data Table 1 | List of the eight CMIP6 models used in this study with their name, institution and spatial resolution

Model	Institute	Nominal Resolution [km]
AWI-CM-1-1-MR	Alfred Wegener Institute, Germany	100
BCC-CSM2-MR	Beijing Climate Center China Meteorological Administration, China	100
CMCC-CM2-SR5	Fondazione Centro Euro-Mediterraneo sui Cambiamenti Climatici, Italy	100
EC-Earth3	EC-Earth Consortium, Europe	100
GFDL-ESM4	National Oceanic and Atmospheric Administration, Geophysical Fluid Dynamics Laboratory, United States	100
MPI-ESM1-2-HR	Max Planck Institute for Meteorology, Germany	100
MRI-AGCM-3-2-H*	Meteorological Research Institute, Japan	60
TaiESM1	Research Center for Environmental Changes, Taiwan	100

*MRI-AGCM-3-2-H is the only model used in this study that belongs to the HighResMIP experiment, whereas the others belong to the SSP585 experiment.

Extended Data Table 2 | Warming levels, averaged over global land and oceans, as estimated by ERA5 for the recent past (1990–2019) and CMIP6 models for the future period (2071–2100); both relative to the baseline period (1950–1979)

Data set	Period	Reference Period	Warming [K]
ERA5*	1990 - 2019	1950 - 1979	0.81
AWI-CM-1-1-MR	2071 - 2100	1950 - 1979	4.78
BCC-CSM2-MR	2071 - 2100	1950 - 1979	4.36
CMCC-CM2-SR5	2071 - 2100	1950 - 1979	5.63
EC-Earth3	2071 - 2100	1950 - 1979	5.88
GFDL-ESM4	2071 - 2100	1950 - 1979	3.86
MPI-ESM1-2-HR	2071 - 2100	1950 - 1979	3.86
MRI-AGCM-3-2-H	2071 - 2100	1950 - 1979	4.94
TaiESM1	2071 - 2100	1950 - 1979	6.64

*ERA5 is the reanalysis data set for the assessment of the recent past whereas the remaining data sets are the CMIP6 model projections.

Extended Data Table 3 | Data sets used for assessing the sensitivity of results to warming levels of 1.5, 2, 3 and 4 K. A total of 43 data sets are used, spanning 7 CMIP6 models and 4 scenarios (ssp126, ssp245, ssp370 and ssp585). Each data set consists of a consecutive 30 years period for which mean global temperature is increased by increments of 1.5, 2, 3 and 4 degrees relative to the baseline period (1950–1979)

Warming [K]	Model	Scenario	Period	Temporal resolution*
1.5	BCC-CSM2-MR	ssp126	2020 - 2049	3 hrs
	BCC-CSM2-MR	ssp245	2018 - 2047	3 hrs
	BCC-CSM2-MR	ssp370	2015 - 2044	3 hrs
	GFDL-ESM4	ssp126	2062 - 2091	daily
	GFDL-ESM4	ssp370	2027 - 2056	daily
	GFDL-ESM4	ssp585	2023 - 2052	daily
	MPI-ESM1-2-HR	ssp126	2070 - 2099	daily
	MPI-ESM1-2-HR	ssp245	2058 - 2087	daily
	MPI-ESM1-2-HR	ssp585	2031 - 2060	daily
2.0	AWI-CM-1-1-MR	ssp126	2070 - 2099	3 hrs
	BCC-CSM2-MR	ssp245	2034 - 2063	3 hrs
	BCC-CSM2-MR	ssp370	2027 - 2056	3 hrs
	BCC-CSM2-MR	ssp585	2023 - 2052	3 hrs
	CMCC-CM2-SR5	ssp245	2022 - 2051	daily
	CMCC-CM2-SR5	ssp370	2023 - 2052	daily
	CMCC-CM2-SR5	ssp585	2017 - 2046	daily
	GFDL-ESM4	ssp370	2039 - 2068	daily
	MPI-ESM1-2-HR	ssp245	2032 - 2061	daily
	MPI-ESM1-2-HR	ssp370	2033 - 2062	daily
	TaiESM1	ssp126	2015 - 2044	3 hrs
	TaiESM1	ssp370	2018 - 2047	3 hrs
3.0	AWI-CM-1-1-MR	ssp370	2066 - 2095	3 hrs
	AWI-CM-1-1-MR	ssp585	2063 - 2092	3 hrs
	BCC-CSM2-MR	ssp370	2050 - 2079	3 hrs
	BCC-CSM2-MR	ssp585	2042 - 2071	daily
	CMCC-CM2-SR5	ssp126	2065 - 2094	daily
	CMCC-CM2-SR5	ssp245	2042 - 2071	daily
	CMCC-CM2-SR5	ssp585	2033 - 2062	daily
	EC-Earth3	ssp245	2037 - 2066	daily
	GFDL-ESM4	ssp370	2061 - 2090	daily
	GFDL-ESM4	ssp585	2056 - 2085	daily
	MPI-ESM1-2-HR	ssp585	2054 - 2083	daily
	TaiESM1	ssp126	2038 - 2067	3 hrs
	TaiESM1	ssp370	2034 - 2063	3 hrs
	TaiESM1	ssp585	2027 - 2056	3 hrs
4.0	BCC-CSM2-MR	ssp585	2063 - 2092	3 hrs
	CMCC-CM2-SR5	ssp245	2070 - 2099	daily
	CMCC-CM2-SR5	ssp370	2062 - 2091	daily
	CMCC-CM2-SR5	ssp585	2048 - 2077	daily
	EC-Earth3	ssp370	2031 - 2060	3 hrs
	EC-Earth3	ssp585	2050 - 2079	3 hrs
	TaiESM1	ssp370	2049 - 2078	3 hrs
	TaiESM1	ssp585	2039 - 2068	3 hrs

*Temporal resolution refers to the highest temporal resolution for which the data set was used in the analysis.